

Deciphering the Cenozoic exhumation history of the Eastern Pyrenees along a crustal-scale normal fault using low-temperature thermochronology

Gaétan Milesi¹, Patrick Monié², Roger Soliva², Philippe Münch³, Pierre G. Valla⁴,
Stéphanie Brichau⁵, Michael Bonno², Céline Martin², and Mathieu Bellanger⁶

¹Chrono-environnement

²Géosciences Montpellier

³Université de Montpellier

⁴University of Grenoble Alpes, University of Savoie Mont Blanc, CNRS, IRD, IFSTTAR, ISTERre

⁵Institut de recherche pour le développement

⁶TLS-GEOTHERMICS

November 22, 2022

Abstract

The timing of transition between the contractional and extensional regimes along the Pyrenean range remains debated. Compared to its central and western parts, the eastern part of the chain was significantly affected by extensional tectonics mostly related to the opening of the Gulf of Lion. The Têt normal fault is the best example of this tectonic activity, with topographic reliefs above 2,000 m in its footwall. In this study, we synthesized previous thermochronological data and performed new (U-Th)/He and fission-track dating in the Eastern Pyrenean massifs. Output apparent exhumation rate and thermal modeling in the hanging-wall of the Têt fault highlight a rapid exhumation (0.48 km/Ma) and cooling ($\sim 30^\circ\text{C}/\text{Ma}$) phase between 38 and 35 Ma, followed by slower exhumation/cooling afterwards. In the footwall, cooling subsequently propagated westward along the fault during Priabonian (35-32 Ma), upper Oligocene and lower Miocene (26-19 Ma), and Serravalian-Tortonian times (12-9 Ma). These data and modeling outcomes suggest that the exhumation of the Têt fault hanging-wall related to southward thrusting ended at 35 Ma, and was followed by different extensional stages, with a propagation of the deformation towards the West during the upper Miocene. We propose that the onset of extension in the Eastern Pyrenees occurred during the late Priabonian period, contemporaneously with the large-scale rifting episode recorded in Western Europe. After this event, the Têt fault activity and the westward propagation of the deformation appear mainly controlled by the opening of the Gulf of Lion.

Hosted file

agusupporting-information_milesi_tectonics.docx available at <https://authorea.com/users/540077/articles/600109-deciphering-the-cenozoic-exhumation-history-of-the-eastern-pyrenees-along-a-crustal-scale-normal-fault-using-low-temperature-thermochronology>

1 **Deciphering the Cenozoic exhumation history of the Eastern Pyrenees along a** 2 **crustal-scale normal fault using low-temperature thermochronology**

3 **G. Milesi^{1,2}, P. Monié¹, R. Soliva¹, P. Münch¹, P.G. Valla³, S. Bricchau⁴, M. Bonno¹,**
4 **C. Martin¹, M. Bellanger⁵**

5 ¹ Géosciences Montpellier, Université de Montpellier, CNRS, Université des Antilles, Montpellier,
6 France

7 ² Chrono-Environnement, UMR 6249-CNRS, Université Bourgogne Franche-Comté, Besançon,
8 France

9 ³ University of Grenoble Alpes, University of Savoie Mont Blanc, CNRS, IRD, IFSTTAR,
10 ISTERre, 38000 Grenoble, France

11 ⁴ Geosciences Environnement Toulouse (GET), Université de Toulouse, UPS, Univ. Paul Sabatier,
12 CNRS, IRD, CNES, 14 av. Edouard Belin, F-31400 Toulouse, France

13 ⁵ TLS Geothermics, 91 chemin de Gabardie, 31200 Toulouse, France

14 Corresponding author: Gaétan Milesi (gaetan.milesi@univ-fcomte.fr)

15 **Key Points:**

- 16 • Tectonic evolution along a major normal fault recorded by low-temperature
17 thermochronology
- 18 • Priabonian (35-32 Ma) switch between contractional and extensional regime in the
19 Eastern Pyrenees
- 20 • Cenozoic westward propagation of the deformation along the Têt fault

21 **Abstract**

22 The timing of transition between the contractional and extensional regimes along the Pyrenean range remains debated.
23 Compared to its central and western parts, the eastern part of the chain was significantly affected by extensional
24 tectonics mostly related to the opening of the Gulf of Lion. The Têt normal fault is the best example of this tectonic
25 activity, with topographic reliefs above 2,000 m in its footwall. In this study, we synthesized previous
26 thermochronological data and performed new (U-Th)/He and fission-track dating in the Eastern Pyrenean massifs.
27 Output apparent exhumation rate and thermal modeling in the hanging-wall of the Têt fault highlight a rapid
28 exhumation (0.48 km/Ma) and cooling (~30°C/Ma) phase between 38 and 35 Ma, followed by slower
29 exhumation/cooling afterwards. In the footwall, cooling subsequently propagated westward along the fault during
30 Priabonian (35-32 Ma), upper Oligocene and lower Miocene (26-19 Ma), and Serravalian-Tortonian times (12-9 Ma).
31 These data and modeling outcomes suggest that the exhumation of the Têt fault hanging-wall related to southward
32 thrusting ended at 35 Ma, and was followed by different extensional stages, with a propagation of the deformation
33 towards the West during the upper Miocene. We propose that the onset of extension in the Eastern Pyrenees occurred
34 during the late Priabonian period, contemporaneously with the large-scale rifting episode recorded in Western Europe.
35 After this event, the Têt fault activity and the westward propagation of the deformation appear mainly controlled by
36 the opening of the Gulf of Lion.

37 **Plain Language Summary**

38 The Pyrenees result from the North-South convergence of the Eurasian and Iberian plates. The eastern part of the
39 range experienced strong extensional tectonics mostly related to the opening of the Gulf of Lion, which timing and
40 influence on the modern topographic relief remain unclear. To better characterize the transition timing between
41 contractional and extensional regimes and the tectonic evolution in the Eastern Pyrenees, we used low-temperature

42 thermochronology and thermal modeling to reconstruct the exhumation/cooling histories of the different massifs along
43 the Têt fault. Our data and modeling outcomes show a switch between contractional and extensional tectonics during
44 the Priabonian (ca. 35 Ma), followed by different extensional stages recorded in the Têt fault footwall, coeval with a
45 global westward propagation of the deformation along the fault until ca. 9 Ma.

46 **1 Introduction**

47 In orogenic belts, crustal-scale faults are key deformation markers that accommodate various regimes of plate tectonics
48 during rock burial, exhumation or strike slip activity (Jones and Wesnousky, 1992; Norris and Cooper, 2001;
49 Ratschbacher et al., 2003; Viola et al., 2004; Malusà et al., 2009). When syn- to post-orogenic sedimentary record or
50 chronological constraints are lacking for bracketting fault activity within orogens, low-temperature (low-T)
51 thermochronology is a powerful tool to quantify the timing and magnitude of exhumation along major faults, since it
52 provides time constraints on the thermal evolution of rocks during their exhumation towards the Earth's surface
53 (Farley, 2002; Ehlers and Farley, 2003; Malusà et al., 2005; Glotzbach et al., 2011; Stockli, 2005; Colgan et al., 2006;
54 Reiners and Brandon, 2006). This situation is common within orogens for which the transition between syn- and post-
55 orogenic periods, or the transition from contraction to extension, remains difficult to date and is often highly debated
56 (Price and Henri, 1984; Carmignani and Kligfield, 1990; Jolivet et al., 2020, 2021a; Séranne et al., 2021). Low-T
57 thermochronology has been widely used in large-scale extensional domains to date the activity of normal faults, as for
58 example in the Basin and Range Province (Foster et al., 1999; Surpless et al., 2002; Armstrong et al., 2003; Colgan et
59 al., 2008) or the Aegean domain (Coutand et al., 2014; Brichau et al., 2006). However, few studies have investigated
60 the onset of post-orogenic extension using low-T thermochronology (i.e. Cederbom et al., 2000; Danišik et al., 2012;
61 Fillon et al., 2021; Martín-González et al., 2012) and even less on the lateral migration of the tectonic activity along
62 normal faults in orogenic context (Deeken et al., 2006, Krugh, 2008; Curry et al., 2016).

63
64 In the Pyrenees, previous thermochronological studies have focused mainly on the central part of the chain, which is
65 composed of a stack of crustal nappes formed during the main Eocene - early Oligocene orogenic build up (Jolivet et
66 al., 2007; Mouthereau et al., 2014; Bosch et al., 2016; Labaume et al., 2016; Vacherat et al., 2016, Waldner et al.,
67 2021). In the eastern part of the Pyrenees, less studies have been carried out (Maurel et al., 2002; 2008; Gunnell et al.,
68 2009), which do not provide a detailed view of fault activity through time. This orogen segment shows a similar nappe
69 structure as further West (Laumonier et al., 2015, 2017; Calvet et al., 2021) but has experienced significant post-
70 orogenic crustal thinning to 25 km of total thickness, as indicated by recent geophysical data (Nercessian et al., 2001;
71 Lacan and Ortuño, 2012; Chevrot et al., 2018; Diaz et al., 2018). This thinning is assigned to the presence of numerous
72 and widely distributed normal faults onshore and offshore (Jolivet et al., 2020, 2021a; Romagny et al., 2020; Calvet
73 et al., 2021, Séranne et al., 2021; Taillefer et al., 2021). The geodynamic origin for the onset of the extension has been
74 linked to either the initiation of the West European Rifting which formed a large intraplate feature (Mouthereau et al.,
75 2021; Angrand and Mouthereau, 2021) or the early onset of back-arc extension leading to the formation of the Gulf
76 of Lion (Séranne, 1999; Séranne et al., 2021) The Têt fault is the most prominent normal fault of the Eastern Pyrenees,
77 which localizes high-relief massifs in its footwall such as the Canigou and Carança (Fig. 1). The development of these
78 high topographic reliefs has been attributed to normal faulting during the Oligo-Miocene period (Maurel et al., 2008).
79 However, the pre-extensional history of this area, the onset of extension and its polyphase activity along strike during
80 the Cenozoic are still poorly understood (e.g. Huyghe et al., 2020; Jolivet et al., 2020, 2021a, 2021b; Angrand and
81 Mouthereau; 2021; Taillefer et al., 2021).

82
83 In this study, we present a new low-T thermochronology dataset from bedrock samples collected on both sides of the
84 Têt fault, including (U-Th)/He on apatite (AHe) and zircon (ZHe), and apatite fission track (AFT). Low-T
85 thermochronological data from previous studies (Maurel et al., 2002; 2008; Gunnell et al., 2009; Milesi et al., 2019;
86 2020a, 2020b) have been also synthesized with the new dataset, and all data are used for thermal modeling to assess
87 the exhumation history of the footwall and hanging wall massifs along the southwestern segment of the Têt fault.
88 Based on these results, we discuss the onset, timing and spatial evolution of Cenozoic extension in the eastern part of
89 the Pyrenees as well as the potential driving mechanisms for this evolution.

90 2 Geological setting

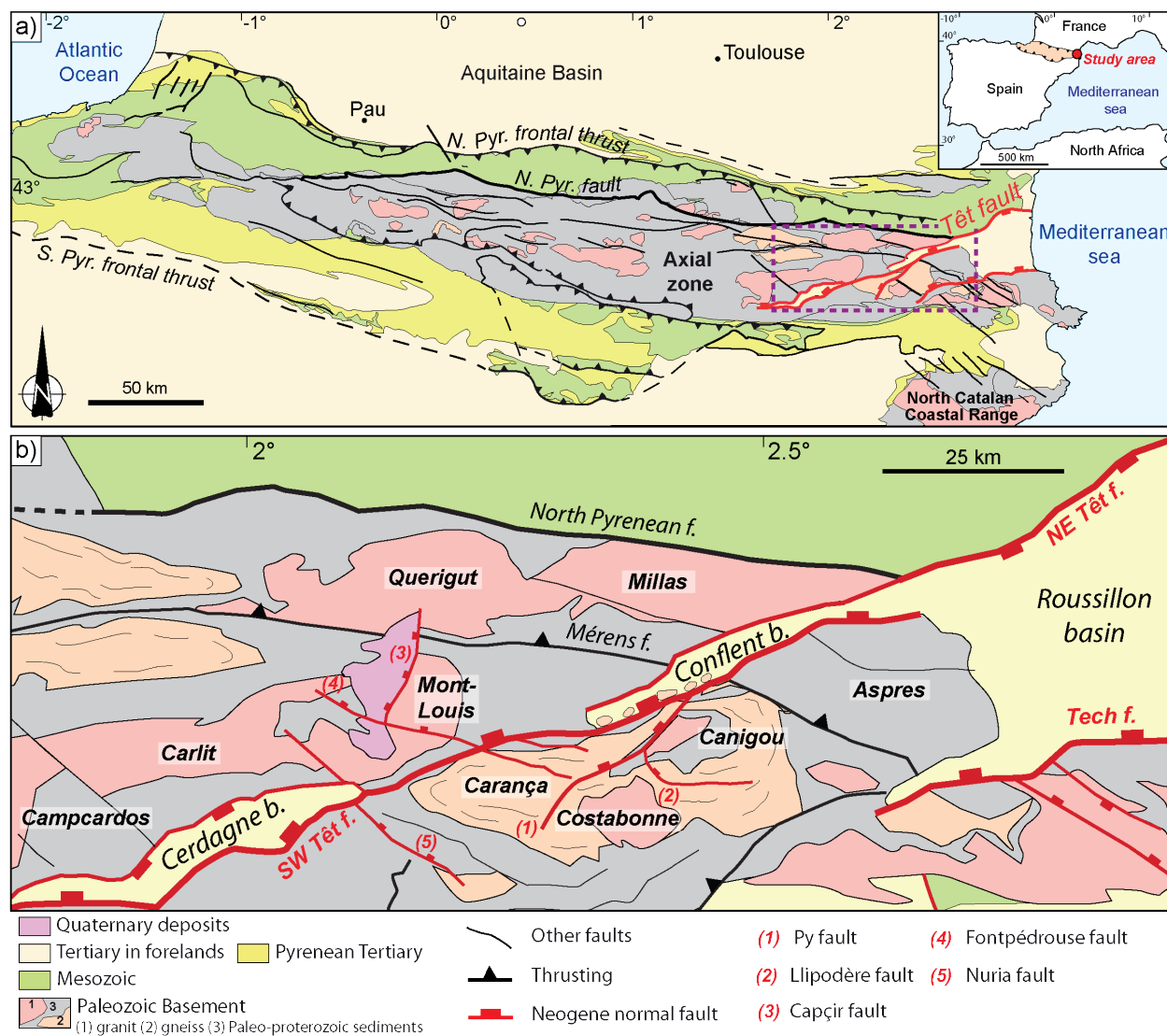
91 2.1 Tectonic evolution of the eastern part of the Pyrenees

92 The Pyrenees result from the North-South convergence of the Eurasian and Iberian plates since the late Cretaceous
 93 (Choukroune et al. 1989; Roure et al. 1989; Muñoz, 1992; Beaumont et al., 2000; Mouthereau et al., 2014; Teixell et
 94 al., 2016), and form a double-wedged mountain range of around 1,000 km long and 150 km wide (Fig. 1a). The
 95 maximum of shortening occurred during the Eocene in the central part of the range (e.g. Vergés et al., 1995; Gibson
 96 et al., 2007; Sinclair et al., 2005; Metcalf et al., 2009; Whitchurch et al., 2011; Fillon and van der Beek, 2012;
 97 Mouthereau et al., 2014; Teixell et al., 2016; Curry et al., 2019). The Pyrenees are divided into three main latitudinal
 98 tectonostratigraphic domains (Vergés et al., 2002; Grool et al., 2018). To the North, three main units are recognized:
 99 the Aquitaine foreland basin, the Sub Pyrenean Zone and the North Pyrenean Zone, the last two being separated by
 100 the North Pyrenean Frontal Thrust (Fig. 1a). Further South, the North Pyrenean Fault (NPF) separates the North
 101 Pyrenean Zone from the Axial Zone and is interpreted as the suture between the Eurasian and Iberian plates. The Axial
 102 Zone consists of a stack of south-verging nappes made of late Proterozoic and Paleozoic sedimentary, metamorphic
 103 and magmatic rocks involved in the Variscan orogeny. The South Pyrenean Zone extends to the South of the Axial
 104 Zone and is composed of a sequence of Mesozoic to Eocene sediments involved in several thrust sheets transported
 105 southward. The Ebro Basin forms the southern foreland basin of the Pyrenean orogen.

106
 107 In the eastern Axial Zone, it is accepted that the mountain building occurred through the emplacement of south-verging
 108 nappes rooted in the northern part of the Axial Zone, south of the NPF (Vergés et al., 1995; Sibuet et al., 2004;
 109 Laumonier et al., 2015; Teixell et al., 2016). In the studied area, the balanced cross sections of Ternois et al. (2019)
 110 suggest an Eocene thrusting of the Aspres–Mont-Louis massifs onto the Canigou massif, in agreement with available
 111 thermochronological data (Maurel et al., 2008). The reactivation of Variscan structures during the Pyrenean orogeny
 112 has been proposed, the most significant example being the Merens fault to the North of our study area (McCaig and
 113 Miller, 1986; Burbank et al., 1992; Guitard et al., 1998; Cochelin et al., 2017; Laumonier et al., 2017). The particularity
 114 of the Eastern Pyrenees is the reactivation of compressional structures during extensional tectonic regime (Séranne et
 115 al., 1995; Séranne 1999; Jolivet et al., 2020, Calvet et al., 2021; Séranne et al., 2021). This regional scale extension is
 116 witnessed by geophysical data that show a progressive crustal thinning, with crustal thickness varying between 45 km
 117 in the eastern part of the Axial Zone (~1°E) to 25 km at the margin of the Gulf of Lion (Chevrot et al., 2018; Diaz et
 118 al., 2018). This regional extensional episode led to the (re-)activation of major structures as normal faults with different
 119 orientations (NE-SW, NW-SE and N-S, Fig. 1b), from the end of the Oligocene to the Quaternary (Taillefer et al.,
 120 2021). Some of these faults have been considered as inherited ductile Variscan faults (Guitard et al., 1992, 1998;
 121 Bouchez and Gleizes, 1995; Autran et al., 2005; Laumonier et al., 2015, 2017). Two main NE-SW trending normal
 122 faults are recognized in the studied area: the Têt and the Tech faults (Fig. 1b). The Têt fault represents the southern
 123 margin of the Cerdagne and Conflent basins, while the Tech fault is the southern bounding fault of the Roussillon
 124 basin. Noteworthy is the importance of a NW-SE trending fault network that affects particularly the Mont-Louis and
 125 Carança massifs (e.g. Fontpédrouse and Nuria faults, Fig. 1.b) and cuts the North Catalan Coastal Range further South
 126 (Fig. 1.a). Some of these faults have nearly E-W directions probably recording spatial and/or temporal changes of
 127 stress orientation and/or stress regime. Major N-S faults in the eastern part of the Pyrenees are rare, among which the
 128 Capçir fault is described as a Quaternary normal fault (Briais et al., 1990). In the study area, the kinematics and amount
 129 of exhumation associated to these different faults are still debated. In Figure 1b, major crustal blocks have been
 130 differentiated and delimited by the Têt fault, namely the Mont-Louis block to the North (hanging wall) and Canigou-
 131 Costabonne and Carança blocks (footwall, delimited by the Py secondary fault) to the South.

132
 133 Previous multi-thermochronological studies (Maurel et al., 2002; 2008; Gunnell et al., 2009) in the Canigou (footwall
 134 of the Têt fault) and Mont-Louis (hanging wall of the Têt fault) provided insights and results guiding our study. Maurel
 135 et al. (2002, 2008) proposed that the Canigou massif was exhumed during two periods, the first one at a rate of ~0.30
 136 km/Ma between 27 and 21 Ma, followed by a significant slowdown of exhumation (~0.10 km/Ma) until present-day.
 137 In the Mont-Louis massif, thermochronological data suggest an earlier exhumation between 50 and 35 Ma (~0.30
 138 km/Ma) accompanied by a rapid cooling. Since 35 Ma, the Mont Louis exhumation has been relatively slow, estimated
 139 at 0.04-0.06 km/Ma (Maurel et al., 2008). These different exhumation and cooling histories between the two massifs
 140 since 35 Ma were interpreted to be related to the normal motion of the Têt fault, without erasing the
 141 thermochronological record of Eocene tectonic activity in the hanging wall. In the Carança massif, thermal modeling
 142 based on AHe data (Milesi et al., 2019a; 2020b) suggests two main cooling events that occurred in the Oligo-Miocene,
 143 a major one between 30 and 24 Ma (at a rate of 25°C/Ma) followed by a second episode between 12 and 9 Ma (at a

144 rate of 15°C/Ma). Despite these previous thermochronological studies, the spatio-temporal evolution of the main tectonic
 145 structures in the eastern part of the Axial Zone of the Pyrenees since the Priabonian remains still poorly constrained
 146 (see Taillefer et al., 2021).
 147



148 **Figure 1.** a) Structural map of the Pyrenees showing the main structural domains delimited by faults (modified after
 149 Taillefer et al., 2017). The major Neogene normal faults of the Eastern Pyrenees are reported in red. The study area is
 150 outlined with an open purple-dashed box. b) Structural sketch map of the study area showing the different massifs (in
 151 bold italics) and basins (in italics) along the Southwestern (SW) and Northeastern (NE) segments of the Têt fault
 152 (modified from Taillefer et al., 2021). Secondary faults are indicated by red numbers (see legend for details).
 153

154 2.2 Tectonic evolution and sedimentary record along the Têt fault

155 The southern segment of the Têt normal fault is a NE-SW north-dipping and 100-km long crustal-scale fault (Maurel
 156 et al., 2002; 2008; Chevrot et al., 2018; Diaz et al., 2018; Fig. 1a). It crosscuts Palaeozoic magmatic and metamorphic
 157 rocks of the Mont Louis, Canigou and Carança massifs along which Neogene sedimentary basins developed (Fig. 1b).
 158 In the Canigou massif, the main period of fault activity during the Oligo-Miocene has been well constrained using
 159 low-T thermochronology (Maurel et al., 2002; 2008). A second stage of normal motion along the entire Têt fault has
 160 been recorded between the middle-Miocene and the late Pliocene, with associated vertical displacements in the range
 161 of 150-500 m (Pous et al., 1986; Rehault et al., 1987; Cabrera et al., 1988; Roca and Desegaulx, 1992; Tassone et al.,

162 1994; Calvet, 1999; Carozza and Baize, 2004; Delcaillau et al., 2004; Agustí et al., 2006; Clauzon et al., 2015) to
 163 kilometric (Calvet, 1996; Mauffret et al. 2001). However, thermochronological data in the Canigou massif (Maurel et
 164 al., 2008) are apparently not consistent with an hypothesis of km-scale vertical displacements. Since the end of
 165 Miocene, a main difference is recorded along the Têt fault between the western (Cerdagne basin) and eastern (Conflent
 166 and Roussillon basins) segments. Indeed, only the western segment of the Têt fault has been active (Calvet, 1999)
 167 which led to the opening of the Cerdagne pull-apart basin accommodated by normal (Pous et al., 1986; Agustí et al.,
 168 2006) and right-lateral displacement along the Têt fault (Cabrera et al., 1988). Based on geomorphological
 169 observations, a westward propagation of the deformation along the Têt fault has also been proposed to occur during
 170 the Plio-Pleistocene (Carozza and Delcaillau, 1999; Carozza and Baize, 2004). The amplitude of Pliocene to
 171 Quaternary normal activity on the eastern segment of the Têt fault is still debated. For some authors, the presence of
 172 triangular facets along the Têt fault scarp documents a recent normal fault activity (Briais et al., 1990; Calvet, 1999).
 173 However, Petit and Mouthereau (2012) suggested these are only the morphological expression of the differential
 174 erosion within Variscan mylonites. It is important to note that facets are also observed on scarps with no apparent
 175 mylonite nor favorably-oriented Variscan foliation (western segment of the Têt fault, Py and Capcir faults, Delmas et
 176 al., 2018). Finally, over the last 6 Ma, low incision rates of maximum 25 m/Ma in the Têt valley indicate weak vertical
 177 uplift in the study area (Sartégou et al., 2018), bringing further evidence to the ongoing discussion on Late-Miocene
 178 potential uplift from paleoelevation studies (Huyghe et al., 2020; Suc and Fauquette, 2012).

179
 180 The sedimentary record is not continuous along the Têt fault system, and three main depositional areas can be
 181 distinguished from East to West: (1) the Roussillon basin bounded to the North by the northern segment of the Têt
 182 fault that is antithetic to the southern segment, (2) the Conflent basin that connects to the Roussillon basin to the East
 183 and (3) the Cerdagne basin along the southwestern segment of the Têt fault (Fig. 1b). The Roussillon basin is a large
 184 graben belonging to the West European Rift system and was highly subsident during the Oligocene-Aquitainian
 185 interval that corresponds to the rifting phase precluding the Liguro-Provençal Sea opening. Post-rift deposits within the
 186 Roussillon basin were deposited in a passive margin geotectonic setting with low tectonic subsidence, and were deeply
 187 incised during the Messinian salinity crisis after which the passive margin sedimentation resumed during the Pliocene
 188 (Clauzon et al., 1987; Clauzon, 1990; Calvet et al., 2015; Calvet et al., 2021). The Conflent basin is an intramontane
 189 half-graben lying along the southwestern segment of the Têt fault, at an elevation ranging from 250 to 1,000 m. Its
 190 sedimentary infill is composed of up to ~1,000 m thick continental deposits, thought to be related to the main tectonic
 191 activity of the Têt fault (Guitard et al., 1998; Calvet et al., 2014). However, the stratigraphy of this basin is debated
 192 and the main sedimentary units, peculiarly an olistostrome with km-scale olistoliths originated from the Canigou
 193 massif, may be either early Burdigalian (Guitard et al., 1998; Calvet et al., 2014) or Pliocene (Clauzon et al., 2015).
 194 Towards the southwest, the Cerdagne basin, at an elevation of 1,100 m, is interpreted as a pull-apart basin formed by
 195 dextral-strike slip along the Têt fault (Cabrera et al., 1988). It has been infilled by 400 to 1,000 m of Neogene sediments
 196 divided in two depositional units from early Miocene and late Miocene, separated by an unconformity (Pous et al.,
 197 1986; Augusti and Roca, 1987; Cabrera et al., 1988; Roca, 1996). The source area of clastic sediments switched from
 198 the North to the South between these two units, with tectonic activity strongly decreasing during the late Miocene
 199 (Roca and Santanach, 1986; Cabrera et al., 1988).

200 **3 Methodology**

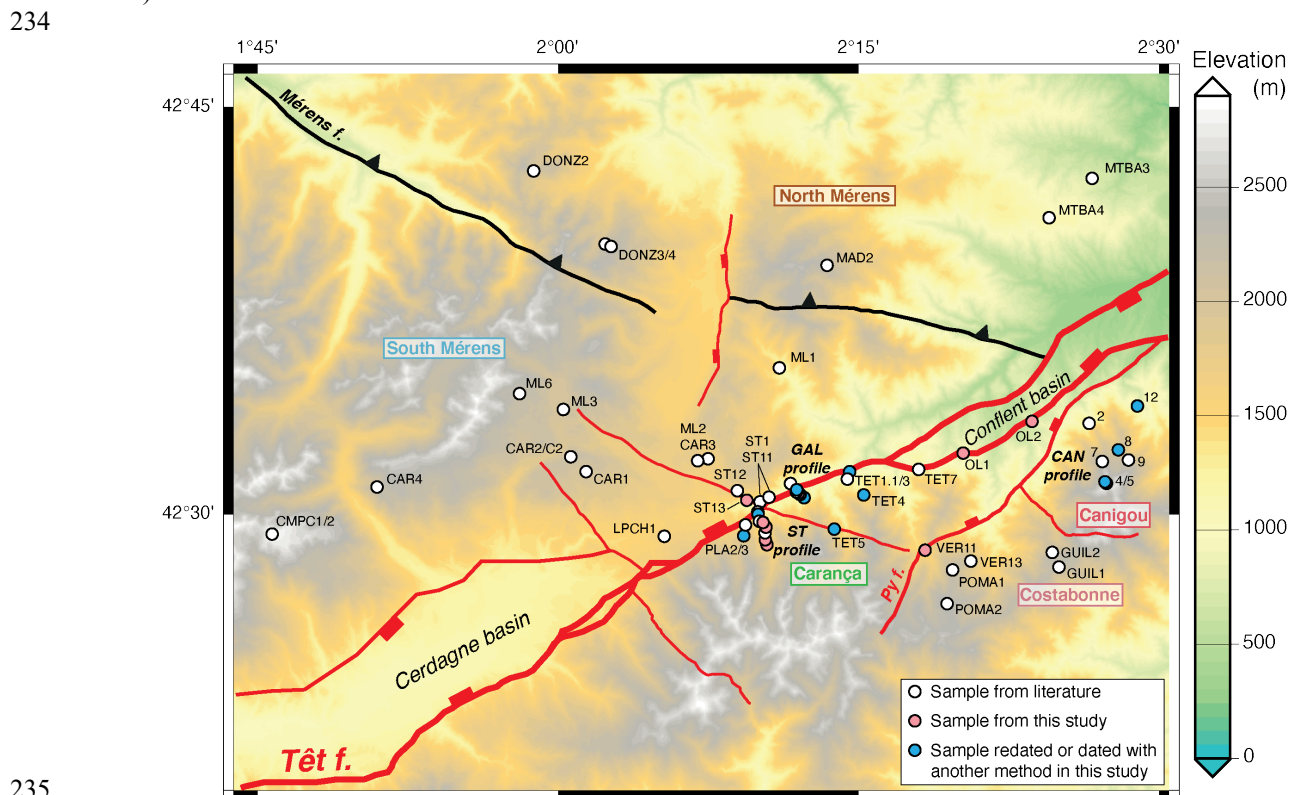
201 **3.1 Low-temperature thermochronology**

202 **3.1.1 Sampling strategy**

203 Our main objective is to quantify the exhumation and thermal evolution of the different crustal blocks separated by
 204 main regional faults, and to provide new data on the kinematic history of these faults. In the hanging wall of the Têt
 205 fault, two main blocks, separated by the Mérens fault, have been studied: respectively the North and South Mérens
 206 blocks. The North Mérens block is composed of the Millas and Querigut granitic massifs, and the South Mérens block
 207 is formed by Mont-Louis, Campcardos and Carlit massifs (Fig. 1b). In the footwall of the Têt fault, two main blocks,
 208 separated by the NE-SW trending Py fault, have been sampled: the Canigou-Costabonne block (eastern segment of
 209 the Têt fault, Canigou and Costabonne sub-blocks separated by the NW-SE Llipodère fault) and the Carança block
 210 (western segment). New AHe, AFT and ZHe ages have been obtained mainly in the footwall of the Têt fault (Carança
 211 and Canigou-Costabonne blocks), which represents a total of 44 AHe ages, 3 AFT ages and 25 ZHe ages (Tables 1
 212 and 2). Thermochronological data from previous studies (Maurel et al., 2008; Gunnell et al., 2009) have been
 213 synthesized and supplemented by AHe ages from our previous studies (Milesi et al., 2019, 2020b). Note that we have

214 excluded samples affected by hydrothermalism and Rare Earth Element mobility, therefore not relevant to define
 215 regional exhumation and thermal evolution of the studied area (Milesi et al., 2019, 2020b, Fig. 2). Sample localities
 216 and corresponding thermochronological data from literature are summarized in Supplementary Section Table S1 and
 217 shown in Figure 2.

218
 219 In the hanging wall of the Têt fault, six samples at an elevation between 730 m and 2,380 m were analyzed in the
 220 North Mérens block (DON, MAD and MTB). The South Mérens block (i.e. Mont-Louis massif) provided seventeen
 221 samples (CAR, CMPC, GAL, LPCH, ML, ST) with an elevation difference of ~1800 m between the lowest sample in
 222 the Têt Valley (1,081 m) and that of the summit of Campcardos (2,900 m). In the footwall of the Têt fault, the
 223 Costabonne massif includes four samples (GUIL and POMA) from Gunnell et al. (2009) and two samples (VER)
 224 dated in this study. In the Canigou massif, Maurel et al. (2008) reported thermochronological data on seven samples
 225 (CAN) collected along a profile from the base of the massif (970 m) to the summit (2,784 m). Three apatite samples
 226 (CAN4, CAN9 and CAN12), initially dated with the AHe population method, have been redated with AHe single
 227 grain method (see section 3.1.2). Two augen gneiss blocks (OL1 and OL2) from the olistostrome formation deposited
 228 in the Conflent basin and originating from the Canigou massif (Clauzon et al., 2015) have been also dated with the
 229 AHe single-grain method. In the Carança block, five new samples have been dated with the AHe method (GAL5, ST6,
 230 ST7, ST9 and ST10) to complete the AHe dataset from Milesi et al. (2019, 2020b). AFT ages have been obtained on
 231 three samples from different sampling profiles (ST2, GAL4 and TET4). Finally, a ZHe age-elevation profile (900 to
 232 1900 m) has been realized with six samples from the Carança block (TET1.1, TET4, TET5, GAL7, GAL3, PLA3 and
 233 ST3).



236 **Figure 2.** Location of samples projected on DEM under GMT (Wessel et al., 2019) using SRTM1s. Different crustal
 237 blocks are delimited by regional major faults. From the North to the South, the sample names are for ST profile : ST2,
 238 ST3, ST4, ST10, ST9, ST8, ST7, ST6 and for GAL profile: GAL7, GAL6, GAL5, GAL4, GAL3, GAL1. Samples
 239 ST2, ST6, ST7, ST9, ST10, GAL4 and GAL5 were dated in this study.

240 3.1.2 Apatite and zircon (U-Th)/He dating

241 Apatite and zircon (U-Th)/He analyses were conducted at the Noble Gas Laboratory of Géosciences Montpellier
 242 (France). All samples were crushed and sieved, and apatite and zircon concentrates were obtained by heavy liquid

243 methods. Inclusion-free crystals with no evidence of fracture were hand-picked under a binocular microscope. Each
 244 single grain was packed in Pt tubes for apatite or Nb tube for zircon, placed under vacuum, and heated with a 1,090-
 245 nm fibre laser operating at 4.0W (900°C) for apatite and 6.2W (1,100°C) for zircon. We applied a duration of heating
 246 of 5 min for apatite and 15 min for zircon. After ³He spiking, gas purification was achieved by a cryogenic trap and
 247 two SAES AP-10-N getters, and helium content was measured on a quadrupole PrismaPlus QMG 220. The ⁴He content
 248 was determined by the peak height method and was 10–10000 times above typical blank levels. A second heating run
 249 using the same analytical procedure was systematically conducted to verify that more than 99% of ⁴He was extracted
 250 during the first run. After helium extraction, Pt or Nb tubes were retrieved from the sample chamber and transferred
 251 in a 2 ml polypropylene conical tube. Samples were doubly spiked (²³⁰Th and ²³³U) and dissolved using procedures
 252 previously described by Wu et al. (2016) for apatite and Gautheron et al. (2021) for zircon. The resulting solutions
 253 were diluted, and U (²³³U and ²³⁸U) and Th (²³⁰Th and ²³²Th) were measured by using isotope dilution ICPMS. For
 254 age calculation, alpha ejection correction (Farley et al., 1996) was calculated using the Ft software (Gautheron and
 255 Tassan-Got, 2010; Ketcham et al., 2011). Durango apatite and Fish Canyon Tuff (FCT) zircon replicates were analysed
 256 between four unknown grains and yielded a mean age of 31.24 ± 2.18 Ma and 29.19 ± 1.19 Ma, respectively, during
 257 the different analyses of this study. These results are consistent with the Durango reference age of 31.02 ± 1.01 Ma
 258 given by McDowell et al. (2005) and FCT reference age of 28.30 ± 2.8 Ma (Reiners and Nicolescu, 2006).
 259 Conservatively, the He Partial Retention Zone (PRZ) for the zircon system is assumed to be between 140°C and 220°C
 260 (Guenther et al., 2013) and in the range of 40°C to 80°C for apatite (Stockli et al., 2000). It is important to note that
 261 the helium retention is sensitive to the crystal chemistry (eU values, chlorine content) and cooling history of samples
 262 (see Ault et al., 2019), and also that the PRZ can spread over a larger range of temperature (see Ault et al., 2019)

263 3.1.3 Apatite fission tracks

264 Apatite grains were mounted and polished for etching to reveal the natural spontaneous fission tracks. Apatites were
 265 etched using 5.5N HNO₃ at 20°C for 20s. Etched grain mounts were packed with mica external detectors and corning
 266 glass (CN5) dosimeters and irradiated in the Chilean CCHEN nuclear reactor. Following irradiation, the external
 267 detectors were etched using 40% HF at 20°C for 40 minutes. Analyses were carried out on an Olympus BX61
 268 microscope at a magnification of $\times 1,250$, using a dry ($\times 100$) objective in the Dating laboratory of Géosciences
 269 Environnement Toulouse (France). Confined track-length measurements were performed using a drawing tube and
 270 digitizing tablet, calibrated against a stage micrometer. Single-grain AFT ages were calculated using the external
 271 detector method and the zeta calibration approach, as recommended by the I.U.G.S. Subcommittee on
 272 Geochronology (Hurford, 1990). Track-length measurements were restricted to confined tracks parallel to the c-
 273 crystallographic axis. Fission tracks in apatite shorten or anneal with increased temperature and duration of heating.
 274 For apatite of typical Durango composition (0.4 wt% Cl), experimental and borehole data (Green et al. 1989; Ketcham
 275 et al. 1999) show that over geologic time fission tracks begin to anneal at a sufficient rate to be measurable above
 276 $\sim 60^\circ\text{C}$, with complete annealing and total resetting of the apatite fission track age occurring between 100 and 120°C.
 277 This range of temperatures is usually labelled the apatite fission-track partial annealing zone (PAZ).

278 3.2 Thermochronological data interpretation

279 3.2.1 Age-elevation relationships (AER)

280 For each crustal block (Fig. 2), the age-elevation relationships (AERs) between the different thermochronological data
 281 have been used to estimate first-order apparent exhumation rates and also to get information on timing for potential
 282 changes in exhumation (i.e. break-in-slope in AERs). This approach is independent from the thermal structure of the
 283 block under consideration (e.g. Wagner et al., 1977; Fitzgerald et al., 1995; Braun, 2002; Fitzgerald and Malusà,
 284 2019), but it relies on several assumptions and simplifications. First, it only considers the measured
 285 thermochronological ages without taking into account potential sample-specific kinetics from parent element content
 286 for instance (e.g. Ault et al., 2019). The AER approach also considers a vertical distribution of investigated samples
 287 (Stüwe et al. 1994), which is rarely the case in the field, and may also be influenced by potential changes in topography
 288 (Braun, 2002) or the presence of secondary faults. A major potential problem concerning the interpretation of AERs
 289 is the complexity of the exhumation scenario (i.e. number of segments which can be defined in an age-elevation
 290 dataset), we thus used a Bayesian Information Criterion (BIC) to select the appropriate model complexity (Schwarz,
 291 1978). In this study, we followed the approach developed by Glotzbach et al. (2011) to determine the best-fitting AER
 292 estimates for AHe, AFT and ZHe data with minimization of the BIC.

293 3.2.2 Inverse thermal modeling under QTQt

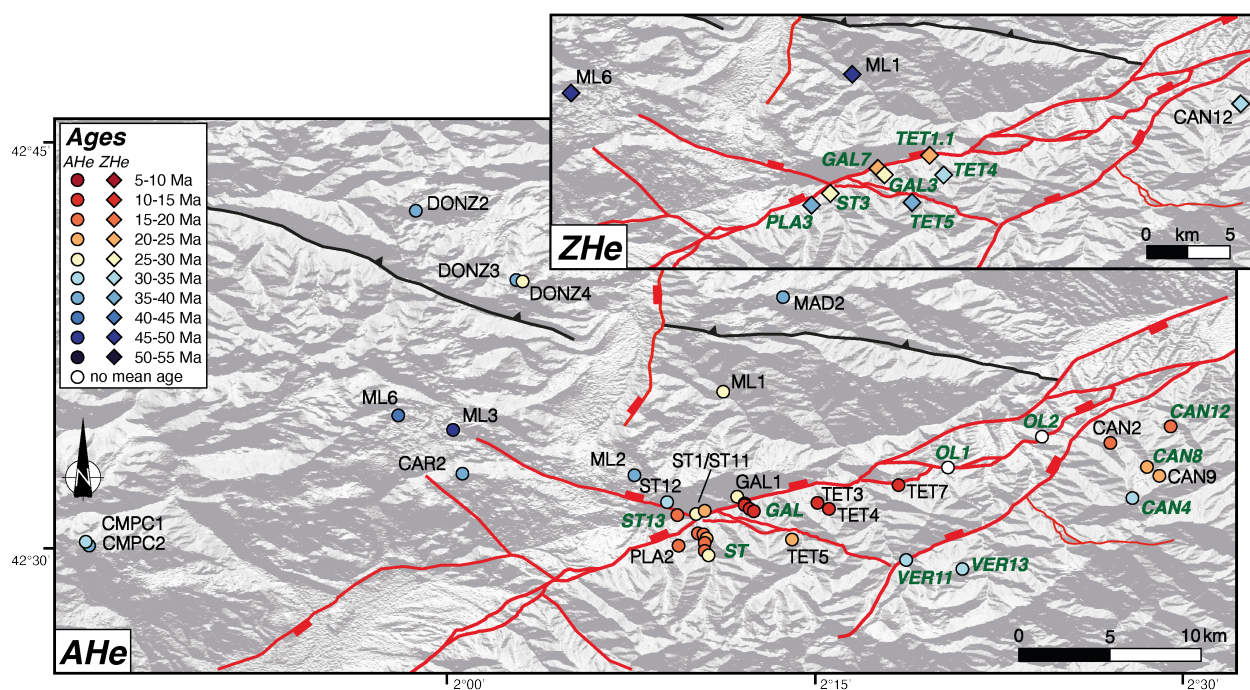
294 In order to reconstruct the thermal history of the different crustal blocks (Fig. 2), time-temperature paths were modeled
 295 with QTQt 5.7.0 software (Gallagher et al., 2009; Gallagher, 2012) using AHe and ZHe single-grain ages and
 296 parameters (eU, Rs) together with AFT single-grain ages with length distribution data. QTQt software uses a Bayesian
 297 Markov chain Monte Carlo (MCMC) sampling method to infer sample time-temperature histories (Sambridge, 1999;
 298 Charvin et al., 2009). This software is particularly efficient to model together several samples from a same elevation
 299 profile. We parametrized modeling to allow all samples of a given elevation profile to evolve under a common thermal
 300 path with a typical geothermal gradient of $30^{\circ}\text{C} \pm 10^{\circ}\text{C}$ in order to take full advantage of the multi-sample inversion
 301 approach (Vermeesch and Tian, 2014). The radiation-damage model of Gautheron et al. (2009) has been chosen for
 302 the AHe, the kinetic models of Ketcham et al. (2007) for AFT and Guenther et al. (2013) diffusion model for ZHe.
 303 For each model, 100,000 iterations have been performed and the predicted vs. observed ages graph is systematically
 304 presented with output time-temperature histories. ZHe data are modeled only for the Carança block (where we
 305 obtained a ZHe elevation profile), and are used as first-order time-temperature constraints to define the thermal
 306 histories of the other crustal blocks (no available ZHe profile, only scarce individual data obtained with the
 307 population method).

308 **4 Results**

309 4.1 New thermochronological ages

310 4.1.1 Apatite and zircon (U-Th)/He

311 All AHe and ZHe single-grain ages obtained in this study are reported in Table 1. We also present different graphs of
 312 ages vs. Rs, eU and Th/U in the Supporting Information (Fig. S1). For the South Mérens block, an augen gneiss
 313 (sample ST13) was collected in the footwall of the Fontpédrouse fault and provides a mean AHe age of 16.7 ± 1.0
 314 Ma. Two apatite grains have not been considered to calculate the mean AHe age due to their anomalous high eU
 315 content compared to the other grains, possibly due to U-rich inclusions in these apatite grains (Table 2 and Fig. S1).
 316 Note that ST13 has an AHe age younger than all AHe ages (all >25 Ma) previously obtained in the South Mérens
 317 block (Maurel et al., 2008; Milesi et al., 2020b). This cannot be explained by different Rs or eU values of the dated
 318 apatite grains (Table 1, Fig. S1) and therefore sample ST13 will be considered independently of other samples from
 319 the South Mérens block due to its particular structural position in the footwall of the Fontpédrouse fault (Fig. 3).
 320



321

322 **Figure 3.** Synthesis of AHe and ZHe ages in the study area. Samples with green and italic labels are new samples
 323 from this study, those with black labels are from previous literature studies (Maurel et al. 2008; Gunnell et al., 2009;
 324 Milesi et al., 2019; 2020a; 2020b). Along altitudinal profiles, samples from North to South are : ST profile - ST3,
 325 ST4, ST10, ST9, ST8, ST7, ST6; GAL profile - GAL7, GAL6, GAL5, GAL3. Samples ST6, ST7, ST9, ST10 and
 326 GAL5 were dated in this study.

327
 328 In the footwall of the Têt fault, three samples from the Canigou massif, previously analyzed using multigrain AHe
 329 approach, were re-processed using a single-grain approach. Sample CAN12 from the base of the profile (970 m) shows
 330 a mean AHe age of 16.7 ± 1.3 Ma that agrees with the multigrain AHe age of 18.8 ± 1.0 Ma (Maurel et al., 2008). On
 331 top of the massif (2,784 m), sample CAN4 displays larger single-grain AHe age dispersion between 24.3 and 33.5
 332 Ma, without any clear relationship with the apatite chemical composition (Table 1 and Fig. S.1). The mean single-
 333 grain AHe age of CAN4 (27.9 ± 4.8 Ma), despite high uncertainty, is younger than the multigrain AHe age of $34.7 \pm$
 334 1.7 Ma obtained on three aliquots by Maurel et al. (2008). At an intermediate elevation (2,050 m), a single apatite
 335 grain provides an AHe age of 19.6 ± 1.0 Ma for sample CAN8. In the southern Costabonne massif, two samples
 336 VER11 (1,560 m) and VER13 (1,935 m) show low intra-sample age dispersion, except one apatite grain excluded for
 337 the mean age calculation due to its important eU content and young AHe age (Table 1 and Fig. S.1). AHe ages are
 338 respectively of 30.6 ± 1.8 Ma for VER11 and 34.9 ± 1.8 Ma for VER13. In the olistostrome of the Conflent basin, two
 339 augen gneisses (OL1 and OL2, Fig. 2) provide five AHe ages with four of them between 40.8 ± 2.3 Ma and $49.5 \pm$
 340 2.2 Ma, and one at 21.7 ± 1.1 Ma. In the Carança massif, a new AHe mean age of 11.9 ± 0.9 Ma has been obtained
 341 for a granite sample (GAL5), thus confirming previous single-grain AHe ages between 10.0 ± 0.4 Ma and 14.1 ± 1.1
 342 Ma obtained for the GAL profile (Milesi et al., 2020b). In the western part of Carança block, samples ST6, ST7, ST9
 343 and ST10 collected at a similar elevation provide mean AHe ages of 25.5 ± 6.5 Ma, 17.1 ± 1.4 Ma, 24.3 ± 3.0 Ma and
 344 19.6 ± 4.4 Ma, respectively (Table 1 and Fig. 3). ST samples provide quite large intra-sample variability in AHe ages,
 345 which cannot be explained by the chemical characteristics (eU, Th/U) or the grain size (Rs).

346
 347 In the Carança massif, seven samples collected at different elevations (from 900 to 1,900 m) have been dated using
 348 the single-grain ZHe method. These zircon grains have an eU content mostly ranging between 500 and 1900 ppm,
 349 except sample PLA2 (1,900 m) that contains two zircons with eU values above 3000 ppm. These samples do not
 350 display important intra-sample age variation and show mean ZHe ages increasing regularly with elevation from 22.0
 351 ± 1.7 Ma to 32.5 ± 3.3 Ma. The two samples PLA3 (1,622 m) and TET5 (1,900 m) from the top of the profile display
 352 similar ZHe ages of 36.2 ± 2.9 Ma and 37.3 ± 3.0 Ma, respectively (Table 1 and Fig. 3).

353 **Table 1.** (U-Th)/He data on apatite and zircon. Single-grain data with * (and in italics) have been considered as
 354 outliers and not considered for the mean age calculation.

Block	Sample/ grain	Rs μm	U ppm	Th ppm	eU ppm	Th/U	4He ncc/g	$\pm s$ ncc/g	Ft	Corrected age Ma	Error $\pm 1\sigma$ (Ma)
Apatite											
South Mérens block	ST13 (42.50727N 2.15867E 1,289m) Augen gneiss										
	ST13a	81.8	12.4	18.6	16.9	1.5	29023.1	1160.9	0.84	17.0	0.8
	ST13b	81.3	14.1	16.0	17.9	1.1	28315.3	849.5	0.85	15.5	0.6
	ST13c	67.0	24.2	24.4	30.0	1.0	49313.1	986.3	0.82	16.7	0.7
	ST13d	59.9	14.3	14.6	17.8	1.0	30276.5	1211.1	0.82	17.2	0.7
	ST13e	61.3	77.2	73.7	94.9	1.0	143789.9	1437.9	0.82	15.4	0.7
	ST13f	45.5	48.5	59.8	62.9	1.2	102885.4	2057.7	0.7	18.1	0.8
	ST13g*	53.3	<i>130.3</i>	<i>158.8</i>	<i>168.4</i>	<i>1.2</i>	<i>356975.6</i>	<i>3569.8</i>	<i>0.8</i>	<i>22.9</i>	<i>1.0</i>
	ST13h*	43.9	<i>94.3</i>	<i>102.8</i>	<i>119.0</i>	<i>1.1</i>	<i>227047.7</i>	<i>2951.6</i>	<i>0.7</i>	<i>21.9</i>	<i>1.1</i>
									Mean	16.7	1.0
Carança block	GAL5 (42.51287N 2.20037E 1,147m) Granite										
	GAL5a	57.3	20.6	5.1	21.8	0.2	19915.4	597.5	0.77	9.8	0.6
	GAL5b	62.7	11.2	5.6	12.5	0.5	15730.0	471.9	0.81	12.9	0.8
	GAL5c	60.8	7.8	2.1	8.4	0.3	10375.3	415.0	0.79	13.0	0.8
									Mean	11.9	1.8
	ST10 (42.4949N 2.17104E 1,383m) Augen gneiss										
	ST10a	61.3	50.1	28.0	56.8	0.6	109832.3	2196.6	0.77	20.9	1.2
	ST10b	56.3	62.3	27.3	68.8	0.4	94741.0	1136.9	0.75	15.3	0.8
	ST10c	75.1	56.1	26.4	62.4	0.5	103165.4	1547.5	0.81	17.0	0.9
	ST10d	67.0	29.1	7.4	30.8	0.3	76314.5	1526.3	0.81	25.2	1.3
									Mean	19.6	4.4
	ST9 (42.49203N 2.17351E 1,421m) Fractured augen gneiss										
	ST9a	60.4	46.6	17.7	50.8	0.4	119148.9	1191.5	0.79	24.7	1.2
	ST9b	68.1	38.6	10.2	41.0	0.3	83334.3	1666.7	0.83	20.4	1.0
	ST9c	68.0	59.8	25.8	66.0	0.4	158824.9	1588.2	0.81	24.5	1.3
	ST9d	63.2	54.0	19.8	58.8	0.4	164830.2	1648.3	0.84	27.8	1.7
									Mean	24.3	3.0
	ST7 (42.48421N 2.17433E 1,494m) Augen gneiss										
	ST7a	61.0	11.3	3.2	12.1	0.3	18475.0	923.8	0.79	16.1	0.8
	ST7b	64.6	16.1	4.6	17.2	0.3	31125.3	1245.0	0.80	18.7	0.9
	ST7c	70.5	24.1	5.9	25.5	0.2	40022.5	800.4	0.82	15.8	0.7
	ST7d	63.5	14.2	3.7	15.1	0.3	26010.2	1040.4	0.80	17.9	0.9
									Mean	17.1	1.4
	ST6 (42.48116N 2.17433E 1,533m) Augen gneiss										
	ST6a	82.1	7.4	2.6	8.1	0.4	27252.5	817.6	0.85	33.1	1.8
ST6b	62.3	13.1	3.3	13.9	0.3	28447.2	1137.9	0.78	21.7	1.1	
ST6c	67.9	7.2	3.3	8.0	0.5	17354.2	867.7	0.82	21.9	1.0	
								Mean	25.5	6.5	
Canigou block	CAN12 (42.56647N 2.48237E 970m) Augen gneiss										
	CAN12a	77.8	32.7	17.4	36.9	0.5	67808.4	678.1	0.84	18.1	0.9
	CAN12b	61.3	32.4	10.6	35.0	0.3	54050.7	540.5	0.83	15.5	0.7
	CAN12c	102.6	8.3	24.1	14.1	2.9	25356.0	253.6	0.90	16.6	0.8
									Mean	16.7	1.3
	CAN8 (42.53956N 2.46652E 2,050m) Augen gneiss										
	CAN8a	80	33.5	2.4	34.1	0.1	67878.1	678.8	0.84	19.6	1.0
	CAN4 (42.51892N 2.45676E 2,784m) Augen gneiss										
	CAN4a	42.6	8.1	17.9	12.4	2.2	25850.1	258.5	0.71	24.3	1.5
	CAN4b	45.1	16.5	43.7	27.0	2.6	62074.6	620.7	0.74	26.0	1.4
	CAN4c	61.7	11.6	35.4	20.1	3.0	64660.9	646.6	0.80	33.5	1.9
									Mean	27.9	4.8
	Costabonne block	VER11 (42.477943N 2.305973E 1,560m) Highly fractured augen gneiss with chlorite									
VER11a		50.0	237.6	17.0	241.7	0.1	639343.3	6393.4	0.75	29.2	1.4
VER11b		47.9	228.1	19.4	232.7	0.1	684958.3	6849.6	0.74	32.7	1.6
VER11c		49.9	153.7	13.2	156.9	0.1	429612.5	4296.1	0.76	29.9	1.5
									Mean	30.6	1.8
VER13 (42.471203N 2.343885E 1,935m) Augen gneiss											
VER13a*		61.9	<i>377.9</i>	<i>156.1</i>	<i>415.3</i>	<i>0.4</i>	<i>969933.9</i>	<i>9699.3</i>	<i>0.81</i>	<i>24.0</i>	<i>1.3</i>
VER13b	52.9	275.0	61.6	289.8	0.2	920151.0	9201.5	0.77	34.3	1.8	
VER13c	57.7	237.9	65.3	253.6	0.3	860128.9	8601.3	0.79	35.4	1.8	
								Mean	34.9	1.8	

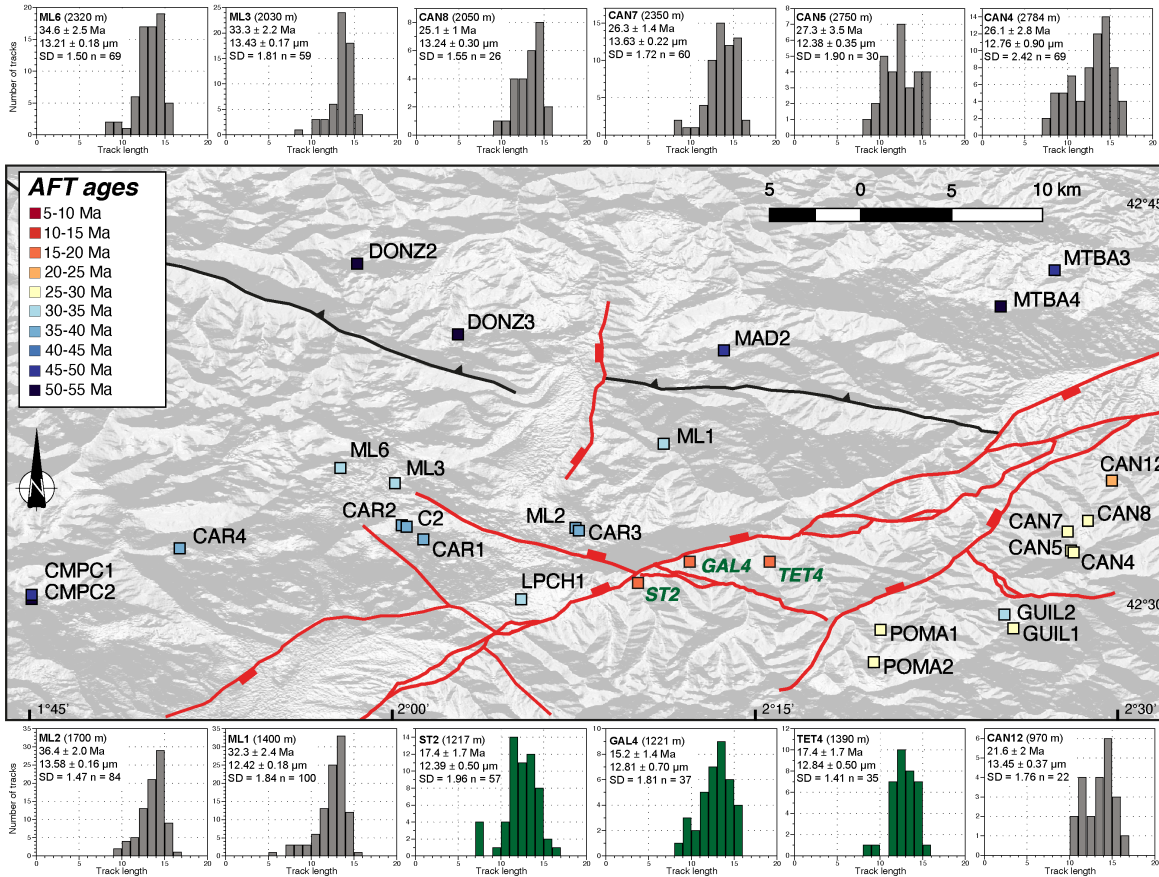
Olistolithes	OL2 (42.55702N 2.39468E 780m) Fractured augen gneiss												
	OL2a	81.2	15.2	9.2	17.4	0.6	76552.5	765.5	0.85	43.1	2.0		
	OL2b	38.6	41.7	49.8	53.7	1.2	100135.0	1001.4	0.71	21.7	1.1		
	OL2c	82.5	13.0	16.3	16.9	1.3	87438.1	874.4	0.87	49.5	2.2		
	OL1 (42.53754N 2.3375E 930m) Fractured augen gneiss												
	OL1a	48.4	17.2	10.7	19.7	0.6	72121.3	721.2	0.71	42.9	2.4		
OL1b	56.7	20.9	9.7	23.2	0.5	88868.5	888.7	0.78	40.8	2.3			
Zircon													
Caraça block	TET1.1 (42.52611N 2.24305555E 900 m) Granite with chlorite												
	TET1.1a	47.9	1185.3	530.6	1312.6	0.4	2188733.2	43774.7	0.70	19.7	1.6		
	TET1.1b	71.0	632.9	201.8	681.3	0.3	1577103.0	41004.7	0.80	23.9	1.9		
	TET1.1c	53.5	525.5	215.5	577.2	0.4	1158414.3	20851.5	0.77	21.6	1.7		
	TET1.1d	54.7	581.0	338.7	662.3	0.6	1397788.4	29353.6	0.77	22.7	1.8		
	Mean											22.0	1.7
	TET 4 (42.51175N 2.25487E 1,390m) Augen gneiss												
	TET4a	73.7	460.9	175.7	503.0	0.4	1449839.5	21747.6	0.83	28.7	2.3		
	TET4b	60.8	548.1	770.2	733.0	1.4	2244859.4	24693.5	0.76	33.5	2.7		
	TET4c	56.1	869.6	320.0	946.4	0.4	3000148.0	48002.4	0.75	35.2	2.8		
	Mean											32.5	3.3
	TET 5 (42.49078N 2.23036E 1,900m) Augen Gneiss												
	TET5a	63.7	564.0	149.9	600.0	0.3	2172324.1	39101.8	0.77	38.9	3.1		
	TET5b	67.8	933.1	423.6	1034.8	0.5	3586410.1	71728.2	0.79	36.3	2.9		
	TET5c	68.5	1192.0	315.4	1267.7	0.3	4567608.3	68514.1	0.82	36.4	2.9		
	TET5d	58.9	968.6	452.4	1077.1	0.5	3262406.1	48936.1	0.76	33.2	2.7		
	Mean											36.2	2.9
	GAL7 (42.51505N 2.19904E 1,025m) Fractured fine grained gneiss with quartz and calcite veins and locally oxides												
	GAL7a	62.4	1090.8	483.6	1206.8	0.4	2620687.7	39310.3	0.80	22.4	1.8		
	GAL7b	54.7	950.0	407.1	1047.7	0.4	2191714.2	39450.9	0.74	23.5	1.9		
	GAL7c	52.3	1264.8	556.2	1398.3	0.4	3105604.0	52795.3	0.77	24.0	1.9		
	Mean											23.3	1.9
	GAL3 (42.51018N 2.20525E 1,363m) Fine grained gneiss												
	GAL3a	55.4	1678.1	328.7	1757.0	0.2	4976741.5	59720.9	0.74	31.6	2.5		
	GAL3b	59.8	685.1	436.9	789.9	0.6	2120801.6	31812.0	0.78	28.6	2.3		
	GAL3c	67.4	685.6	477.6	800.3	0.7	2144053.6	40737.0	0.81	27.5	2.2		
	GAL3d	66.0	881.9	207.1	931.6	0.2	2581295.1	41300.7	0.78	29.4	2.3		
	Mean											29.3	2.3
	ST3 (42.50001N 2.16697E 1,174m) Unaltered gneiss with biotite												
	ST3a	59.9	1316.3	557.5	1450.2	0.4	3801126.6	49414.6	0.76	28.6	2.3		
	ST3b	63.4	1802.8	314.4	1878.2	0.2	4910004.5	68740.1	0.77	28.0	2.2		
	ST3c	61.3	1121.4	661.1	1280.0	0.6	2993707.8	47899.3	0.77	25.3	2.0		
Mean											27.3	2.2	
PLA3 (42.49343N 2.15462E 1,622 m) Fractured leucoeratic gneiss and locally oxidized													
PLA3a	49.5	2958.1	226.3	3012.4	0.1	9898474.3	89086.3	0.75	36.2	2.9			
PLA3b	50.4	3478.6	417.7	3578.8	0.1	11888683.1	106998.1	0.75	36.8	2.9			
PLA3c	61.3	1678.8	277.0	1745.2	0.2	6282251.9	50258.0	0.77	38.9	3.1			
Mean											37.3	3.0	
Note. Ft: Alpha ejection correction (Farley et al., 1996)													

356

357

4.1.2 Apatite fission tracks (AFT)

358 In the Caraça massif, three new AFT ages have been obtained for samples TET4 (1,390 m) and GAL4 (1,221 m) and
 359 ST2 (1,217 m) (Fig. 4). They are respectively of 17.4 ± 1.7 Ma, 15.2 ± 1.4 Ma and 17.4 ± 1.7 Ma, with related mean
 360 track lengths of 12.84 ± 0.50 μm , 12.81 ± 0.70 μm and 12.39 ± 0.50 μm . AFT data and mean track lengths are
 361 summarized in Table 2 and shown with literature data on Figure 4.



362

363 **Figure 4.** AFT central ages for the study area. Samples ST2, GAL4 and TET4 (in green) are from this study, AFT
 364 ages in black have been extracted from Maurel et al. (2008) and Gunnell et al. (2009) (See Supplementary Table S1
 365 for details and locations).

Sample (elevation)	No. of crystals	Track density ($\times 10^6$ tr.cm $^{-2}$)			Age dispersion		U (ppm)	Central age (Ma $\pm 1\sigma$)	Mean track length (μ m)	StD (μ m)	No. of tracks measured
		ρ_d [Nd]	ρ_s [Ns]	ρ_i [Ni]	RE (%)	$P\chi^2$ (%)					
TET4 1,390 m	10	1.183 [10391]	0.400 [119]	4.546 [1377]	0.1	67.37	48.0	17.4 \pm 1.7	12.84 \pm 0.5	1.81	35
GAL4 1,221 m	16	1.189 [10391]	0.333 [163]	4.659 [2203]	14.7	17.14	49.0	15.20 \pm 1.4	12.81 \pm 0.7	2.53	40
ST2 1,217 m	20	1.177 [10391]	0.307 [150]	3.601 [1741]	17.6	28.01	38.3	17.4 \pm 1.7	12.39 \pm 0.5	2.46	57

366

367 **Table 2.** Fission-track data for the Carana massif. Analyses were determined by the external detector method using
 368 0.5 for the $4\pi/2\pi$ geometry correction factor. Apatite fission-track ages were calculated using dosimeter glass (CN-5;
 369 Analyst Stephanie Brichau, $\xi=341.8\pm 7.8$) calibrated by multiple analyses of IUGS apatite age standards (Hurford,
 370 1990). $P\chi^2$ is probability of obtaining χ^2 value for ν degrees of freedom, where ν is the amount of crystals. Central
 371 age is a modal age, weighted for different precisions of individual crystals. In track density, ρ_d is the fission track

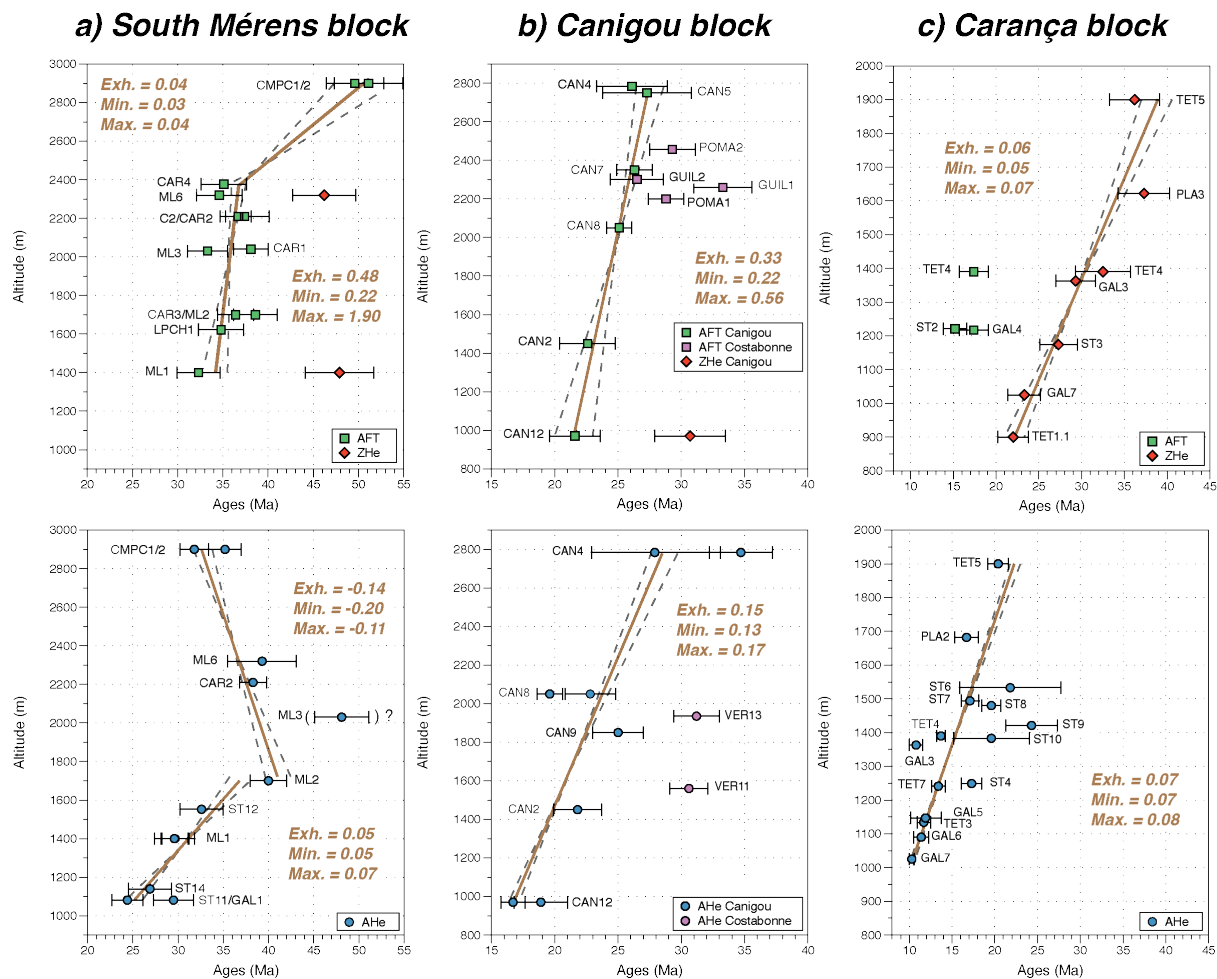
372 density of the standard U-glass (CN-5); Ns (spontaneous), Ni (induced) and Nd (dosemeter) are the fission track
373 numbers corresponding to ρ_s , ρ_i and ρ_d , respectively.

374 4.2 AERs and apparent exhumation rates

375 4.2.1 Hanging wall of the Têt fault

376 In the hanging wall of the Têt fault, AERs are presented only for the South Mérens block (Fig. 5a). AERs based on
377 AFT and AHe data suggest a three-stage exhumation scenario defined by the lowest BIC (Fig. 5a). Samples between
378 1,400 m and 2,400 m provide AFT central ages between 32.3 ± 3.4 Ma and 38.6 ± 2.4 Ma, corresponding to a mean
379 apparent exhumation rate of 0.48 km/Ma. The uncertainty on this exhumation rate is relatively large (from 0.22 to
380 1.90 km/Ma) because most samples lie on an apparent vertical straight line. Samples CMPC1 and CMPC2 from the
381 top of the profile (2,900 m), with AFT central ages ~ 50 Ma, indicate a lower apparent exhumation rate (0.04 km/Ma)
382 that prevailed between ~ 35 and 50 Ma (Fig. 5a, upper graph); although the two ZHe ages in this block suggest potential
383 variability in the exhumation rate during this period. CMPC1 and CMPC2 are the westernmost samples, it may also
384 be possible that they have experienced different exhumation than other samples further East. However, these are the
385 only thermochronological data available above 2,400 m for the South Mérens block, so we cannot assess further this
386 potential difference.

387
388 AHe ages from samples above 1,700 m indicate an apparent negative exhumation rate between 35 and 40 Ma. Sample
389 ML3 (2,030 m), which presents an AHe mean age older than its AFT central age has not been considered. This age
390 inversion can find several explanations: an excess helium in the apatite grains (Green et al., 2006), the presence of
391 inclusion inside or rich U-Th grain boundary phases (Murray et al., 2014). Sample ST13 is not presented in the Figure
392 5, its mean AHe age (16.7 ± 1.0 Ma) is younger than that of other samples and cannot be explained by the regional
393 AER trend. The particular structural location of this sample in the footwall of the Fontpédrouse fault, close to the fault
394 corner between Fontpédrouse (NW-SE) and the Têt fault (NE-SW) can explain the specific exhumation history due
395 to the NW-SE fault activity (see Section 2.1). The negative apparent exhumation rate obtained can be due to: (1) the
396 small number of samples (4 in total) above 1,700 m used to precisely define an exhumation rate in this block; (2) a
397 change in AHe kinetics due to the rapid exhumation (e.g Ault et al., 2019); (3) a major decrease of relief during this
398 period (Braun, 2002; Reiners, 2007; McDannell et al., 2014). This AER above 1,700 m is strongly influenced by AHe
399 mean ages from CMPC1/2 samples at the top of the profile (Fig. 5a, lower graph), and can be explained only by rapid
400 exhumation rates, consistently with the exhumation rates derived from the AFT central ages during this period (Fig.
401 5a, upper graph). Samples between 1,000 m and 1,700 m (Fig. 5a, lower graph) provide AHe mean ages between 24.2
402 ± 4.0 Ma and 40.0 ± 2.0 Ma, suggesting an important decrease in the apparent exhumation rate (0.05 km/Ma). For
403 comparison, AFT ages in the North Mérens block support a mean apparent exhumation rate of 0.46 km/Ma between
404 ~ 52 and 48 Ma, with high uncertainty due to the low number of AFT central ages obtained for this block (see
405 Supporting Information Fig. S2).
406



407

408 **Figure 5.** Age-Elevation Relationships (AERs) for AFT and ZHe (first row) and AHe data (second row) for (a) the
 409 South Mérens block (the AHe mean age of sample ML3 at elevation of 2,050 m, with AHe mean age older than AFT
 410 central age has not been considered), (b) the Canigou-Costabonne massif and (c) the Carança massif.

411

412 4.2.2 Footwall of the Têt fault

413 In the footwall of the Têt fault, the Canigou-Costabonne (Fig. 5b) and Carança blocks (Fig. 5c) are separated by the
 414 Py fault and therefore their AERs have been considered individually. On Figure 5b (upper graph), the AER deduced
 415 from AFT data in the Canigou sub-block (between 970 m and 2,784 m), suggests a single exhumation phase between
 416 ca. 22 and 27 Ma, with an apparent exhumation rate of 0.33 km/Ma. AHe mean ages from the same block (Fig. 5b,
 417 lower graph) are between 16.7 ± 1.8 Ma and 34.7 ± 2.5 Ma, suggesting an apparent exhumation rate of 0.16 km/Ma
 418 from the Priabonian to the end of the Burdigalian. South of the Canigou massif, samples from the Costabonne massif
 419 do not show enough elevation difference to provide a reliable exhumation rate from AERs. However, it can be noted
 420 that for samples taken at similar elevations in these two massifs, the AFT and AHe ages are 1 to 10 Ma older in the
 421 Costabonne massif than in the Canigou massif (Fig. 5b).

422

423 In the Carança massif (Fig. 5c), both ZHe and AHe data have been used to constrain apparent exhumation rates from
 424 AERs. Three AFT central ages cannot be used given the limited elevation distribution (Fig. 5c, upper graph). ZHe
 425 data obtained on 7 samples show a quasi-ideal AER with an apparent exhumation rate of 0.06 km/Ma between ca. 37
 426 and 22 Ma. AHe data suggest a similar apparent exhumation rate (0.07 km/Ma), between ca. 22 and 10 Ma, with some
 427 age variability for samples between 1,250 and 1,550 m on the ST profile, probably due to the proximity of secondary
 428 NW-SE faults that locally fragmented the massif in many sub-blocks (Fig. 5c, lower graph). We can also note that the

429 AER slope defined between 17 and 15 Ma by the three AFT central ages of the Carança block is in agreement with
430 that derived from AHe mean ages from 20 to 10 Ma (Fig. 5c).

431 4.3 Thermal evolution

432 4.3.1 Hanging-wall of the Têt fault

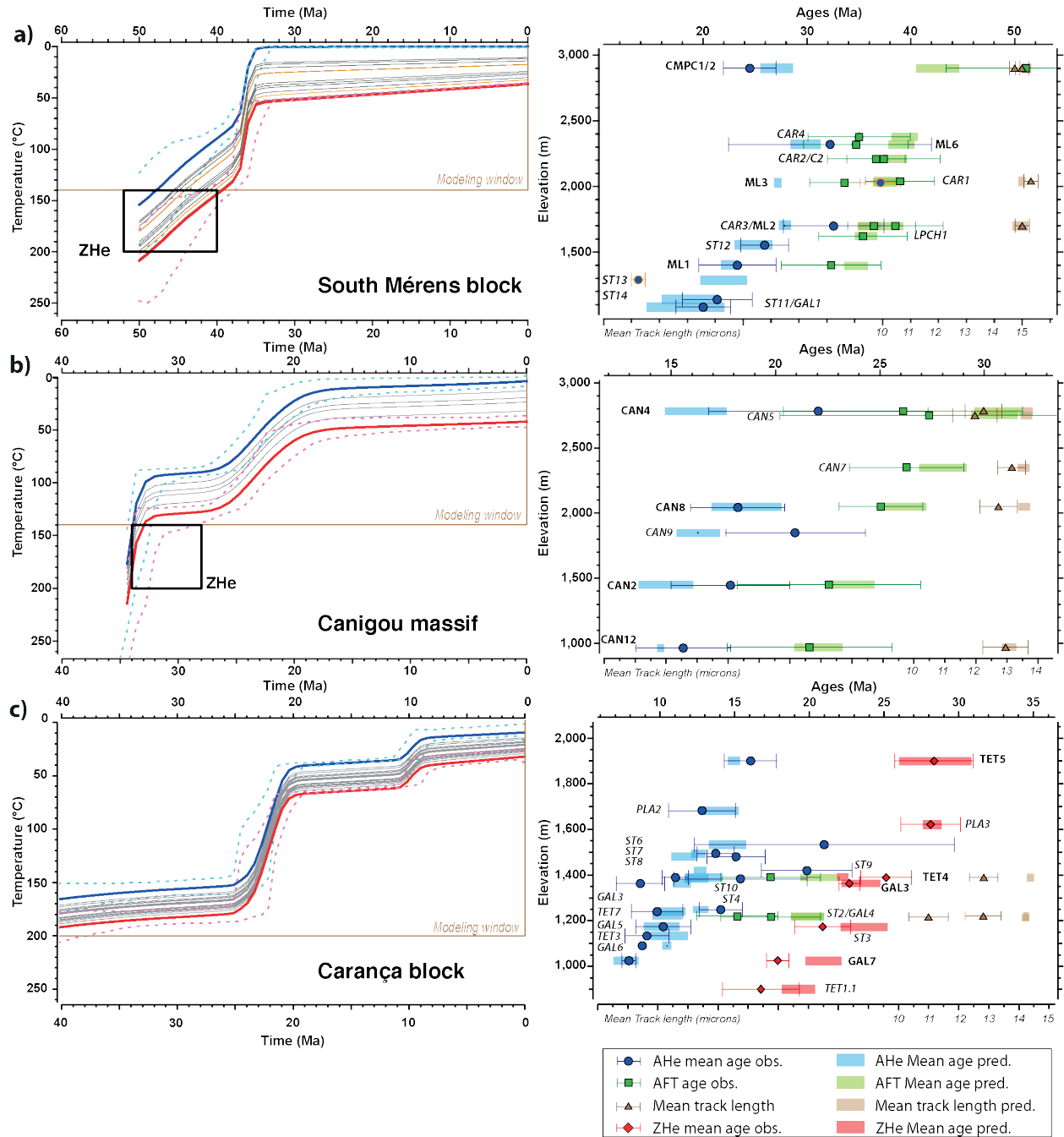
433 The thermal history of the South Mérens block has been derived for all AHe (30) and AFT (12) data from 16 samples
434 used to define AERs (Fig. 5a). For this block, the two ZHe ages of samples ML1 and ML6 (Fig. 3) have been used as
435 time-temperature constraints for numerical modeling. Another model set-up, including AHe ages of ST13 and ML3
436 samples and without any ZHe constraint, has been considered and is presented in the Supporting Information (Figure
437 S3). The output thermal evolution, depicted on Figure 6a, shows that between 50 and 38 Ma, the South Mérens block
438 experienced a cooling rate of around 5°C/Ma, followed by an abrupt acceleration in cooling (~30°C/Ma) between 38
439 and 35 Ma. Then, since 35 Ma, this block was experiencing slow and continuous cooling (<1°C/Ma). Similar results
440 have been observed in the alternative model (Supporting Information Figure S3), while AHe ages of ST13 and ML3
441 samples cannot be correctly reproduced (Figure S3). With the exception of two AHe ages, all predicted AHe, AFT
442 ages and track lengths are consistent with the observed data implemented for inverse modeling (Fig. 6a).

443 4.3.2 Footwall of the Têt fault

444 For the Têt footwall, QTQt thermal modeling was conducted successively on the Canigou and Carança blocks, which
445 are separated by the Py fault. In the Canigou block, data available in the Costabonne sub-block were not considered
446 due to the presence of the Llipodère fault between the Canigou and Costabonne sub-blocks (Fig. 1b) and the lack of
447 data under 2,200 m (only 2 samples with AHe method, VER11 and VER13). An alternative modeling set-up with data
448 from Costabonne sub-block is available in the Supporting Information (Fig. S3). The Canigou thermal modeling (Fig.
449 6b) was designed with all the AHe (12), AFT (6) and track-length data from 7 samples available from the bottom to
450 the top of the massif (thermal modeling output without ZHe constraint is available in the Supporting Information,
451 Figure S3). The output thermal history suggests an important cooling event until ca. 33 Ma (onset timing not precisely
452 constrained) at around 30°C/Ma, followed by slow cooling (<1°C/Ma) until ca. 26 Ma. A second cooling phase at
453 ~10°C/Ma can be observed between 26 and 19 Ma, followed by slow cooling until present-day. The thermal history
454 reproduces well AHe, AFT ages and mean track lengths, except the AHe age of sample CAN9 (2,100 m) and mean
455 track lengths measured on samples from the Canigou summit (CAN4 and CAN5). Thermal modeling based on data
456 from the Costabonne sub-block (Supporting Information, Figure S3) also suggests rapid cooling (30°C/Ma) for this
457 block between 32 and 29 Ma, followed by slow cooling (<1°C/Ma); however this model output should be considered
458 with caution due to the small amount of data (4 AFT and 2 AHe). This rapid cooling would be consistent with an early
459 Oligocene cooling phase, before the Oligo-Miocene phase recorded between 26 and 19 Ma for the Canigou massif
460 (Fig. 6b).

461
462 The modeled thermal history of the Carança block (Fig. 6c) is based on AHe (59), AFT (3) and ZHe (24) data from
463 20 samples. Output thermal history reveals slow cooling (<1°C/Ma) of the massif between 40 and 25 Ma. The main
464 cooling phase at ~20°C/Ma occurred between 25 and 21 Ma, followed by slow cooling (<1°C/Ma) until 12 Ma. A
465 second cooling pulse, of relatively minor magnitude, can be observed between 12 and 9 Ma with a predicted cooling
466 rate of 10°C/Ma, and is followed by slow cooling (<1°C/Ma) since 9 Ma. Despite the important amount of data and
467 an apparent dispersion of AHe ages (see Fig. 6c), the modeled thermal history reproduces well the AHe ages (except
468 for samples GAL6, GAL3, ST6 and ST9), AFT ages and ZHe ages (except for sample GAL7). However, we can note
469 that the predicted mean track lengths are not well reproduced and are generally longer than the observed ones (Fig.
470 6c).

471



472

473 **Figure 6.** Thermal history of (a) South Mérens block from the hanging wall of the Têt fault, (b) Canigou massif and
 474 (c) Carança block from the footwall of the Têt fault. Thermal models were computed using QTQt software (Gallagher,
 475 2012). T-t paths for the uppermost (blue) and the lowermost (red) samples are presented (dashed lines correspond to
 476 95 % confidence interval). Black boxes are constraints based on ZHe data from South Mérens block and Canigou
 477 massif, ZHe data are modeled for the Carança block. To the right, age-elevation profiles using predicted vs. observed
 478 ages for each block are presented as well as observed and predicted track lengths. AHe ages represented with orange
 479 error bars in the South Mérens block are not used to construct the thermal evolution model. Sample names for which
 480 several thermochronometers were used are indicated in bold. Note that mean predicted/observed data are presented

481 for clarity, but that thermal modeling has been using/predicting single-grain AHe/ZHe data and (U-Th)/He ages
 482 (uncorrected for alpha ejection; Farley et al., 1996).

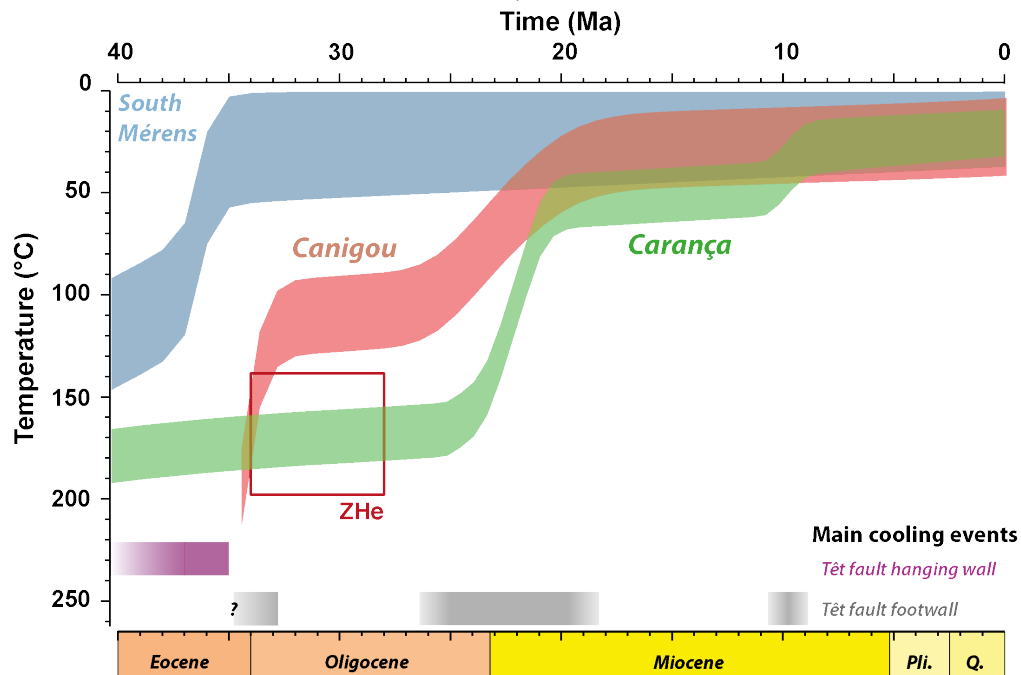
483 5 Discussion

484 5.1 The Têt fault hanging wall: contractional stage

485 In the hanging wall of the Têt fault, North and South Mérens blocks were distinguished in the present study. In the
 486 North Mérens block, AHe mean ages are between 30 and 40 Ma (Fig. 3), while AFT central ages are between 45 and
 487 54 Ma (Figs. 4 and S3). These ages are older than those obtained at similar elevations in the South Mérens block. This
 488 difference in low-T thermochronological data suggests an early exhumation of the North Mérens block during the
 489 Early Eocene, which is in agreement with McCaig and Miller (1986), who proposed on the basis of $^{40}\text{Ar}/^{39}\text{Ar}$ mica
 490 dating that the Mérens fault was reactivated southward around 50-60 Ma. The scarcity of data in the North Mérens
 491 block has not allowed to perform thermal modeling.

492
 493 The thermal history of the South Mérens block (Fig. 6a), obtained using AHe and AFT data, highlights a first stage of
 494 cooling between 50 and 38 Ma ($> 5^\circ\text{C}/\text{Ma}$), that is coeval with a period of maximum shortening in the Eastern Pyrenees
 495 that has been evidenced in the Agly-Salvezines massifs to the North of our study area (Ternois et al., 2019). This
 496 cooling stage became more rapid between 38 and 35 Ma ($\sim 30^\circ\text{C}/\text{Ma}$, Fig. 6a). The fast exhumation rate that prevailed
 497 during this last cooling stage (0.45 km/Ma from AER, Fig. 5a) can be associated with the activity of the Cadi-Canigou
 498 thrust fault that emerges further South (Ternois et al., 2019). This thrust is one of the major fault accommodating the
 499 convergence between the Iberian and European plates during the Eocene (also see Fitzgerald et al., 1999; Whitchurch
 500 et al., 2011; Rushlow et al., 2013; Mouthereau et al., 2014; Bosch et al., 2016; Labaume et al., 2016; Cruset et al.,
 501 2020). This interpretation is also consistent with the general propagation and stacking of the nappes from the North to
 502 the South in the Pyrenees (Jolivet et al., 2007; Fillon and van der Beek, 2012; Cruset et al., 2020).

503
 504 At around 35 Ma, our thermal model output suggests that nearly all the samples collected from 1100 m to 2900 m
 505 were above their respective PAZ and PRZ. After 35 Ma, low cooling rates are consistent with an important decrease
 506 in exhumation towards present-day in the Têt-fault hanging wall (Fig. 5a). This is in agreement with the recent
 507 exhumation model for the Axial Zone proposed by Curry et al. (2021). On the basis of a regional thermochronological
 508 data compilation and thermo-kinematic modeling (for details see Curry et al. 2011), this exhumation model suggests
 509 that rock uplift rates peak at 30-40 Ma in the Eastern Pyrenees, about 10 Ma earlier than in the western Pyrenees (see
 510 also Fillon and van der Beek, 2012 for a similar conclusion).



511

512 **Figure 7.** Output thermal histories for the study area: the South Mérens block (blue), the Canigou massif (red, with
 513 the associated box for ZHe constraint) and the Carança block (green). Thermal models were computed using QTQt
 514 software (Gallagher, 2012). Main cooling events are indicated by purple (hanging wall of the Têt fault) and grey
 515 (footwall of the Têt fault) bars.

516 5.2 The Têt fault footwall : extensional stage

517 In the different crustal blocks from the southern Têt fault footwall, we used a large number of ZHe, AFT and AHe
 518 data to constrain output thermal histories that emphasize multiple cooling phases since the end of the Eocene. (Fig.
 519 7). A first fast cooling ($\sim 25^{\circ}\text{C}/\text{Ma}$), that started at an unconstrained period but ended at ca. 33 Ma, is recorded
 520 essentially by samples from the top of the Canigou massif (CAN4 and CAN5). Within these two samples, the
 521 differences between modeled and observed mean track lengths (Fig. 6b) can be explained by the the small amount of
 522 measured tracks ($n= 30$ and 69 , respectively, see Fig. 4). We can note that zircon fission-track ages of Maurel et al.
 523 (2008) from the top and bottom of the Canigou massif are very similar (30.9 ± 2.5 Ma and 33.8 ± 2.1 Ma respectively,
 524 see Supporting Information Table S1). This suggests an important exhumation step of at least 2,000 m during the
 525 Priabonian-Rupelian period, which is not recorded further West in the Carança block by the ZHe data (Fig. 5c).
 526 Thermochronological data from the Costabonne massif are also consistent with an early Rupelian cooling phase in
 527 the Py fault footwall (Supporting Information Figure S3). The Py normal fault is a NW dipping master fault between
 528 the Canigou and Costabonne massifs (with numerous field evidence of substantial displacement : triangular facets,
 529 metric fault core with gouges) that branches out on the Têt fault to the North (Fig. 1 and 2).

530
 531 This important exhumation signal in the Canigou and Costabonne massifs is better explained by normal faulting rather
 532 than south-verging thrusting at regional scale, such as described further South of the study area (e.g. Cruset et al.,
 533 2020). We propose that this interpretation of exhumation before 33 Ma is only relevant to the Canigou and Costabonne
 534 massifs (Figs. 1 and 6) and not to the whole Canigou-Carança range in agreement with Ternois et al. (2019). The Têt
 535 and Py faults had probably both accommodated the main exhumation of the Canigou and Costabonne blocks, the
 536 normal activity of the Py fault (or both faults) resulting in maintaining the Carança block at depth to the West. Normal
 537 activity of the western part of the Têt fault (Carança block) cannot be excluded due to the connection between the Py
 538 and the Têt faults (Fig. 1). The normal activity of the Py fault thus explains why the low-T thermochronometers used
 539 in our study do not record any cooling below PRZ nor PAZ during this period in the Carança block. In a contractional
 540 context, the diachronism between the Canigou and Carança blocks would require the presence of a master reverse
 541 back-thrust between these two blocks, which is not supported by field observations along the Py fault. Because the
 542 South Mérens block was already at shallow crustal level and thus has not recorded any significant cooling/exhumation
 543 since 35 Ma, both the Py fault and the southeasternmost segment of the Têt fault were probably active during the
 544 Priabonian-Rupelian period to allow for the exhumation of the Canigou-Costabonne massifs only.

545
 546 The second major cooling event from our output thermal histories occurred between the upper Oligocene and the
 547 lower Miocene (i.e. ca. 26 to 19 Ma), and was recorded by both the Canigou and the Carança massifs (Fig. 7). During
 548 this period, the Canigou massif experienced relatively fast exhumation (0.33 km/Ma from AER, Fig. 5b). This
 549 cooling/exhumation signal can be thus associated to normal faulting all along the Têt fault. In the Canigou massif,
 550 low-T thermochronology data do not document any major cooling/exhumation since 19 Ma, suggesting that the
 551 southeastern segment of the Têt fault remained partly inactive since the Burdigalian. This is in agreement with the
 552 sedimentary record in the Conflent basin, showing that the main subsidence, associated with normal activity of the
 553 eastern segment of the Têt fault, was concentrated from the Aquitanian to the Early Burdigalian (Calvet et al., 2014).
 554 In addition, the AHe mean ages (mostly older than 40 Ma) obtained on gneiss samples from the olistotrome formation
 555 in the Conflent basin suggest that the olistolithes collapsed during this upper Oligocene–lower Miocene phase of
 556 significant exhumation. Indeed, AHe mean ages from the olistotrome formation are older than for modern bedrock
 557 samples at the top of the Canigou profile (AHe mean ages about 30 Ma, Fig. 5b). These old ages also show that the
 558 olistolithes were not buried enough to reset the AHe signal.

559
 560 In the Carança block, our AHe data allow to differentiate two sub-blocks separated by the NW-SE Fontpédrouse fault
 561 (Figs. 1 and 3). AHe mean ages from the eastern sub-block (TET and GAL samples) are younger (10-15 Ma) than for
 562 the western sub-block (ST and PLA samples) collected at similar elevations (15-25 Ma, Fig. 3). This AHe age
 563 difference is obvious for samples between 1,250 and 1,550 m (Fig. 5c). In addition, the Fontpédrouse normal fault
 564 propagates in the South Mérens block, and it seems likely that the AHe mean age of 16.7 ± 1.0 Ma obtained close to
 565 this fault (sample ST13) recorded the fault activity during the Burdigalian (see also alternative thermal modeling in

Supporting Information, Figure S3). Note that despite the proximity of a huge gouge zone and evidence for fluid alteration, the Rare Earth Element distribution of this sample remains unaffected by hydrothermalism (see Supporting Information, Figure S4) compared to our previous observations along the Têt fault itself (Milesi et al., 2020b). NW-SE trending faults are frequent in this western segment of the Têt fault (see Milesi, 2020; Taillefer et al., 2021) and their activity can account for an important segmentation of the Carança massif with therefore a spatial variability in AHe data due to slightly different cooling histories within the different sub-blocks. In spite of these local perturbations by NW-SE faults in the Carança block, AHe and ZHe data are well reproduced by the QTQt model (Fig. 6c), and only mean track lengths show important differences between observed and modeled data, which can be explained by the small amount of tracks measured on the three samples (see Table 2 for details).

A third cooling event has been recorded between 12 and 9 Ma (Serravalian-Tortonian) but only for the Carança block (Fig. 7). The lack of record in the Canigou-Costabonne and South Mérens crustal blocks suggests a tectonic activity limited to the southwestern segment of the Têt fault, rather than a general exhumation of the eastern part of the Pyrenees (Huyghe et al., 2020; Calvet et al., 2021). This relatively recent activity can explain the preservation of triangular facets along the Têt fault (Petit and Mouthereau, 2012; Delmas et al., 2018) and is also consistent with the syntectonic sedimentation of late-Miocene age recorded by the lower unit in the Cerdagne basin (Pous et al., 1986; Augusti and Roca, 1987; Roca, 1996). The opening of the Cerdagne pull-apart sedimentary basins appears essentially controlled by the development of the NW-SE normal faults, facilitated by pre-existing NW-SE segments along the Têt fault (Cabrera et al., 1988).

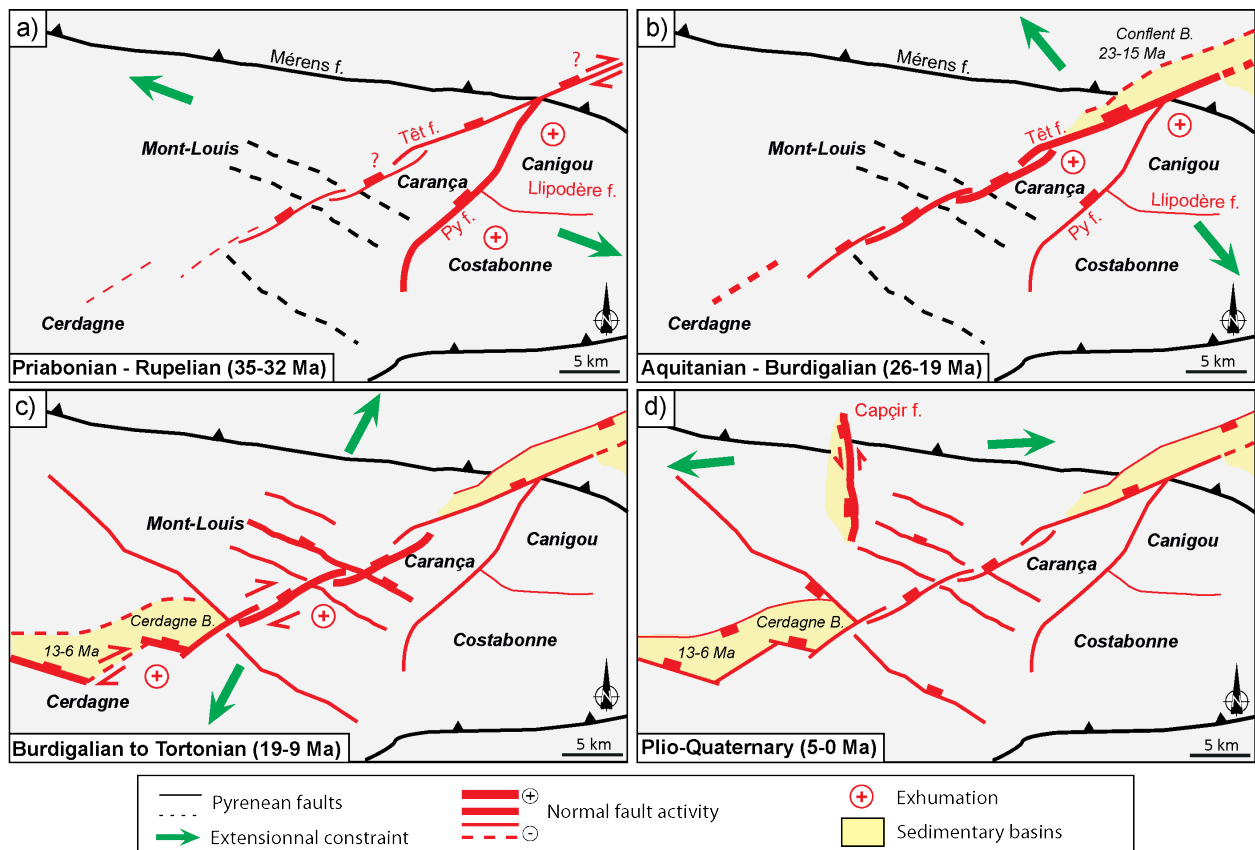
5.3 Fault system evolution model and geodynamic implications

In the eastern part of the Pyrenees, North-South shortening has been recorded until ca. 35 Ma by our low-T thermochronological data. This is consistent with the timing for late contractional episode on the North Pyrenean Thrust Front (Grool et al., 2018) and the last main peak of pyrenean activity (Bartonian-Priabonian) recorded in Provence (Lacombe and Jolivet, 2005). On another side, new U-Pb on calcite studies suggest that shortening in the external units of the Pyrenees proceeded until the middle Miocene (Cruset et al., 2020; Hoareau et al., 2021; Parizot et al., 2021), which could be a consequence of the far field stress imposed by Africa-Europe convergence (Jolivet et al., 2021b; Mouthereau et al., 2021). Based on the sedimentary record, a recent study in the Gulf of Lion margin revealed that the shift between the pyrenean contractional and extensional tectonics occurred during the late Rupelian (~30 Ma, Séranne et al., 2021), with evidence for a rapid change in the tectonic regime. Although the timing of this shift in tectonic regime is globally consistent (see Section 5.2), our results suggest a slightly earlier onset of normal faulting along the Py and Têt faults, i.e. during the Priabonian, and an end of extensional tectonics at ca. 33 Ma (Fig. 7). We should also note that previous thermochronological studies proposed a large-scale episode of exhumation recorded in the Eastern Pyrenees between 35 Ma and 30 Ma (Morris et al., 1998) that could be regarded as a consequence of normal faulting, rather than thrusting. This first extensional event preceded a ~7 Ma long period of exhumation quiescence between 33 and 26 Ma (Fig. 7), which is synchronous to the development of back-arc extension in the Mediterranean domain (onset at 32–30 Ma, Jolivet and Faccenna, 2000). Thus the first exhumation and coeval extensional tectonic phase does not appear to be related to the rifting phase leading to the opening of the Liguro-Provençal domain, especially with regard to the specific configuration of the Py fault (Fig. 8a, i.e. oriented N030E compared to the N060E main trend of the Gulf of Lion faults). This event may rather correspond to the West European Rifting from strain geometry and age of exhumation (Ziegler, 1992; Romagny et al., 2020; Angrand and Mouthereau, 2021; Jolivet et al., 2021b; Mouthereau et al., 2021; Séranne et al., 2021). The West European Rifting is considered geodynamically independent and can lead or be immediately followed by the Gulf of Lion opening (Réhault et al., 1984; Séranne, 1999; Vignaroli et al., 2008; Jolivet et al., 2015, 2020).

A second extensional event has been recorded between the upper Oligocene and Burdigalian for the whole Canigou-Carança range, associated to a main normal faulting phase along the Têt fault (Figs. 7 and 8b). This event corresponds to the main cooling event recorded by Maurel et al. (2008), and it appears to be related to the opening of the Gulf of Lion, consistently with sedimentary records on the Catalan margin (Bartrina et al., 1992). In terms of direction of extension (NW-SE), this event clearly corresponds to the NE-SW trend of the faults observed in the Languedoc, Roussillon, Catalan and Valencia troughs, as well as offshore faults observed at the margin of the Gulf of Lion (e.g. Séranne, 1999; Mauffret et al., 2001; Maillard et al., 2020; Romagny et al., 2020; Jolivet et al., 2021a). In terms of timing, this second extensional event appears slightly younger than the onset of rifting in Languedoc (late Rupelian, Séranne, 1999), and earlier than the second stage of normal faulting on the Catalan margin (Roca and Desegaulx, 1992), probably reflecting the rift propagation towards the Southwest (Séranne, 1999).

620
 621
 622
 623
 624
 625
 626
 627
 628
 629
 630
 631
 632
 633
 634
 635
 636
 637
 638
 639
 640
 641
 642
 643

A third extensional event (Fig. 8c) has been recorded by AHe data in the Carança and the South Mérens blocks, not in the Canigou-Costabonne block (Fig. 3). In the Carança massif, AHe data suggest a change in the direction of extension from NW-SE to NE-SW during the Lower-Miocene times (ca. 18 Ma), with normal-sense movement on the NW-SE Fontpédrouse fault. This stage evolved afterwards between 12 and 9 Ma on the southwestern segment of the Têt fault, commonly associated to a reactivation stage with moderate normal displacements between 150 and 500 m (Pous et al., 1986; Clauzon et al., 1987; Rehault et al., 1987; Roca and Desegaulx, 1992; Tassone et al., 1994; Calvet, 1999; Carozza and Baize, 2004; Delcaillau et al., 2004; Agustí et al., 2006; Clauzon et al., 2015). AHe data along the Têt fault reveal that the exhumation was probably more pronounced along the southwestern segment (>500 m). This stage, that is not recorded by low-T thermochronology data in the Canigou massif (Maurel et al., 2008, this study), marks differential exhumation along the Têt fault, more pronounced at this stage in the southwestern part, consistently with sediment infills of the Cerdagne basin (Pous et al., 1986; Agustí et al., 2006). This late activity on the southwestern segment of the Têt fault confirms the southwestward propagation of the exhumation along the Têt fault (Carozza and Delcaillau, 1999; Carozza and Baize 2004). The direction of extension is also consistent with Middle-Miocene to Pliocene normal faulting in the Emporda basin and the North-Catalan Ranges that trends globally NW-SE (Medialdea et al., 1994; Saula et al., 1994; Tassone et al., 1994; Lewis et al., 2000; Taillefer et al., 2021). Moreover, the pull-apart opening of the Cerdagne basin, accommodated by normal activity of NW-SE to E-W faults (Pous et al., 1986; Agustí et al., 2006) and right-lateral displacements on NE-SW faults (Cabrera et al., 1988), suggests that the main direction of extension was NNE-SSW, allowing the NE-SW Têt fault to be reactivated in right-lateral strike-slip movement (Fig. 8, Cabrera et al., 1988, Goula et al., 1999; Carozza and Baize, 2004, Delcaillau et al., 2004). We should also note that this trend of extension is also compatible with the stress tensors obtained in the Cerdagne area by Cruset et al. (2020). NW-SE faults could therefore have contributed to the uplift of the Cerdagne basin during Middle Miocene (Huyghe et al., 2020; Calvet et al., 2021; Tosal et al., 2021).



644

645 **Figure 8.** Reconstitution of the extensional tectonic evolution since the Priabonian in the eastern part of the
 646 Pyrenees. a) Priabonian-Rupelian period (35-32 Ma) is marked by the exhumation of the Canigou-Costabonne massif,
 647 linked to the Py fault normal motion. A WNW-ESE direction of extension is proposed. b) Aquitanian-Burdigalian

648 period (26-19 Ma) is characterized by the opening of the Gulf of Lion and normal motion of the Têt fault, more
 649 pronounced on the eastern segment of the fault. This observation is in agreement with the early formation of the
 650 Conflent basin at 23 Ma. During this period, the Têt fault normal activity is associated to a change towards the North
 651 of extensional direction c) Burdigalian to Tortonian period (19-9 Ma) reveals a propagation further West of the
 652 exhumation along the Têt fault with late cooling event recorded for the Carança massif. Local (re-)activation of the
 653 NW-SE faults can be involved in AHe dispersion for this block. To the West, the formation of the Cerdagne basin
 654 during the Serravalian (13 Ma) is consistent with a spatial migration of the tectonic activity. Normal activity of the
 655 NW-SE faults and NE-SW Têt fault is possible under NNE-SSW extension. d) Plio-Quaternary period (5-0 Ma) is
 656 marked by a N-S fault activation (Capçir f.) and E-W direction of extension (Calvet, 1999; Rigo et al., 2015).
 657

658 This Lower-Miocene change in direction of extension could be related to geodynamic processes implying stress
 659 changes at the Mediterranean domain scale. Romagny et al. (2020) proposed a global change in the main direction of
 660 slab retreat at about 20 Ma, with a change in the direction of retreat from NNW-SSE to mostly E-W towards the
 661 Apennines. Although at far distance from our study area and not clearly kinematically consistent, such process
 662 involving mantle flux perturbations may have implied stress changes at far distances in the Pyrenean lithosphere.
 663 Another potential source of stress perturbation could be the mechanical interaction and linkage (e.g. Crider and
 664 Pollard, 1998; Kattenhorn et al., 2000) between the Cevennes and the Catalan lithospheric normal faults, through a
 665 very large-scale relay zone located in the Eastern Pyrenees. Such large-scale mechanical interaction could have
 666 favoured stress changes and strain distribution along multiple faults in this eastern part of the Pyrenees. Linkage had
 667 to develop with new NW-SE relay faults after the growth of the two NE-SW Cevennes and Penedes master faults in
 668 the Oligocene – Lower Miocene (e.g. Seranne et al., 1999), consistently with the timing and direction of the Upper
 669 Miocene NW-SE faults observed in the study area. Also note that both master fault segmentation at the place of the
 670 pre-existing Pyrenees and the timing of linkage are consistent with the margin development in the Roussillon and its
 671 specific orientation (NNW-SSE) in the Gulf of Lion (Mauffret et al., 2001). Finally, another hypothesis to consider is
 672 the presence of an new extensional phase due to a not well known geodynamic process in the area (e.g. stresses due
 673 to wedge collapse, erosion, or new mantle dynamic, etc.) in a larger domain since a similar cooling event has been
 674 recorded in the western Axial Zone (Fillon et al., 2021).
 675

676 During the Plio-quaternary period (Fig. 8d), seismic data inversion highlight a global N-S contraction in the area,
 677 while we can note E-W extension in the Cerdagne basin (Rigo et al., 2015). This E-W extension can be responsible
 678 for the Capçir N-S normal faulting (Calvet, 1999; Baize et al., 2002), kinematically consistent with a recent return to
 679 N-S Pyrenean contraction in the study area.

680 **6 Conclusions**

681 Low-temperature thermochronology and inverse thermal modeling reveal successive cooling periods associated to the
 682 differential exhumation of crustal blocks along the southern Têt fault. In the hanging wall of the Têt fault, low-T
 683 thermochronological data indicate a significant exhumation/cooling period ($\sim 30^{\circ}\text{C}/\text{Ma}$) between 38 and 35 Ma,
 684 followed by an important decrease in exhumation/cooling ($< 1^{\circ}\text{C}/\text{Ma}$). This slowdown is interpreted as the result of
 685 the last Pyrenean contractional stage during the Priabonian. In the Têt fault footwall, we propose that an early
 686 exhumation stage of the Canigou-Costabonne block is recorded until 33 Ma ($\sim 30^{\circ}\text{C}/\text{Ma}$) but not in the Carança block
 687 (further West), in association to the normal activity of both the Têt and Py faults. These results suggest a rapid switch
 688 between contractional and extensional regime in the Eastern Pyrénées during the Priabonian. A second major cooling
 689 event ($\sim 20^{\circ}\text{C}/\text{Ma}$) between the Upper Oligocene and Lower Miocene (26-19 Ma) is recorded both in the Canigou and
 690 Carança massifs, associated to the major period of activity of the Têt fault linked to the opening of the Gulf of Lion.
 691 During the upper Miocene, low-T thermochronological data from solely the Carança massif suggest a third cooling
 692 event ($\sim 10^{\circ}\text{C}/\text{Ma}$) during the Serravalian-Tortonian (12-9 Ma) and its segmentation in different sub-blocks separated
 693 by NW-SE faults. Our results reveal a progressive propagation of the deformation towards the Southwest along the
 694 Têt fault, and also account for major changes in the direction of extension in the Eastern Pyrenees since the Priabonian.

695 **Acknowledgments, Samples, and Data**

696 **Competing interests.** The authors declare that they have no conflict of interest.
 697

698 **Data availability.** All the data used in this study can be obtained in the figures, references, and supporting informa-
 699 tion. The data are deposited in Geochron database (<https://www.geochron.org>).

700
701
702
703
704
705
706
707
708
709
710

Acknowledgements. Thanks for technical support go to Olivier Bruguier, Lucie Koeller and Léa Causse for ICP-MS analyses, and Cyprien Astoury for apatite and zircon separation. Thanks to V. Combaudon and G. de Montbrun for help during Canigou sampling and apatite preparation for dating and Frédéric Mouthereau and Riccardo Asti for their positive remarks and improvements. P.G.V. acknowledges funding support from the Swiss National Science Foundation SNSF (Grant PP00P2_170559) and the French ANR-PIA program (ANR-18-MPGA-0006). This research received funding from the programme TelluS of the Institut National des Sciences de l'Univers, CNRS.

Financial support. This research has been supported by the THERMOFAULT, a project supported by the Region Occitanie (France) involving TLS Geothermics (main sponsor), Géosciences Montpellier, and the TelluS Program of CNRS/INSU.

711 **References**

- 712
713 Agustí, J., Oms, O., Furió, M., Pérez-Vila, M.-J., & Roca, E. (2006). The Messinian terrestrial record in the Pyrenees:
714 The case of Can Vilella (Cerdanya Basin). *Palaeogeography, Palaeoclimatology, Palaeoecology*, 238(1–4), 179–189.
715 <https://doi.org/10.1016/j.palaeo.2006.03.024>
716
- 717 Angrand, P., & Mouthereau, F. (2021). Evolution of the Alpine orogenic belts in the Western Mediterranean region
718 as resolved by the kinematics of the Europe-Africa diffuse plate boundary. *BSGF - Earth Sciences Bulletin*, 192, 42.
719 <https://doi.org/10.1051/bsgf/2021031>
720
- 721 Armstrong, P. A., Ehlers, T. A., Chapman, D. S., Farley, K. A., & Kamp, P. J. J. (2003). Exhumation of the central
722 Wasatch Mountains, Utah: 1. Patterns and timing of exhumation deduced from low-temperature thermochronology
723 data. *Journal of Geophysical Research: Solid Earth*, 108(B3). <https://doi.org/10.1029/2001JB001708>
724
- 725 Ault, A. K., Gautheron, C., & King, G. E. (2019). Innovations in (U–Th)/He, Fission Track, and Trapped Charge
726 Thermochronometry with Applications to Earthquakes, Weathering, Surface-Mantle Connections, and the Growth
727 and Decay of Mountains. *Tectonics*, 38(11), 3705–3739. <https://doi.org/10.1029/2018TC005312>
728
- 729 Autran, A., Calvet, M., Delmas, M. (2005). Carte géologique de la France à 1/50 000, feuille mont-louis. BRGM.
730
- 731 Bartrina, M. T., Cabrera, L., Jurado, M. J., Guimerà, J., & Roca, E. (1992). Evolution of the central Catalan margin
732 of the Valencia trough (western Mediterranean). *Tectonophysics*, 203(1–4), 219–247. [https://doi.org/10.1016/0040-
733 1951\(92\)90225-U](https://doi.org/10.1016/0040-1951(92)90225-U)
734
- 735 Beaumont, C., Muñoz, J. A., Hamilton, J., & Fullsack, P. (2000). Factors controlling the Alpine evolution of the
736 central Pyrenees inferred from a comparison of observations and geodynamical models. *Journal of Geophysical
737 Research: Solid Earth*, 105(B4), 8121–8145. <https://doi.org/10.1029/1999JB900390>
738
- 739 Bosch, G. V., Teixell, A., Jolivet, M., Labaume, P., Stockli, D., Domènech, M., & Monié, P. (2016a). Timing of
740 Eocene–Miocene thrust activity in the Western Axial Zone and Chaînons Béarnais (west-central Pyrenees) revealed
741 by multi-method thermochronology. *Comptes Rendus Geoscience*, 348(3–4), 246–256.
742 <https://doi.org/10.1016/j.crte.2016.01.001>
743
- 744 Bouchez, J. L., & Gleizes, G. (1995). Two-stage deformation of the Mont-Louis-Andorra granite pluton (Variscan
745 Pyrenees) inferred from magnetic susceptibility anisotropy. *Journal of the Geological Society*, 152(4), 669–679.
746 <https://doi.org/10.1144/gsjgs.152.4.0669>
747
- 748 Braun, J. (2002). Quantifying the effect of recent relief changes on age–elevation relationships. *Earth and Planetary
749 Science Letters*, 200(3–4), 331–343. [https://doi.org/10.1016/S0012-821X\(02\)00638-6](https://doi.org/10.1016/S0012-821X(02)00638-6)
750
- 751 Briaies, A., Armijo, R., Winter, T., Tapponnier, P., Herbecq, A. (1990). Morphological evidence for quaternary normal
752 faulting and seismic hazard in the eastern pyrenees. *Ann. Tecton.* 4, 19–42.
753
- 754 Brichau, S., Ring, U., Ketcham, R. A., Carter, A., Stockli, D., & Brunel, M. (2006). Constraining the long-term
755 evolution of the slip rate for a major extensional fault system in the central Aegean, Greece, using thermochronology.
756 *Earth and Planetary Science Letters*, 241(1–2), 293–306. <https://doi.org/10.1016/j.epsl.2005.09.065>
757
- 758 Burbank, D. W., Puigdefàbregas, C., & Muñoz, J. A. (1992). The chronology of the Eocene tectonic and stratigraphic
759 development of the eastern Pyrenean foreland basin, northeast Spain. *Geological Society of America Bulletin*, 20.
760
- 761 Cabrera, L., Roca, E., & Santanach, P. (1988). Basin formation at the end of a strike-slip fault: the Cerdanya Basin
762 (eastern Pyrenees). *Journal of the Geological Society*, 145(2), 261–268. <https://doi.org/10.1144/gsjgs.145.2.0261>
763
- 764 Calvet, M. (1996). Morphogenèse d'une montagne méditerranéenne, les pyrénées orientales (vol. 1, 1170 p).
765 University of Paris, Paris.

- 766
767 Calvet, M. (1999). Régimes des contraintes et volumes de relief dans l'est des Pyrénées/Stress regimes and volumes
768 of reliefs in the Eastern Pyrenees. *Géomorphologie: relief, processus, environnement*, 5(3), 253–278.
769 <https://doi.org/10.3406/morfo.1999.991>
770
- 771 Calvet, M., Gunnell, Y., & Delmas, M. (2014). The Têt River Valley: A Condensed Record of Long-Term Landscape
772 Evolution in the Pyrenees. In M. Fort & M.-F. André (Eds.), *Landscapes and Landforms of France* (pp. 127–138).
773 Dordrecht: Springer Netherlands. https://doi.org/10.1007/978-94-007-7022-5_13
774
- 775 Calvet, M., Autran, A., Wiazemsky, M., Laumonier, B., Guitard, G. (2015). Carte géologique de la France, 1:50,000
776 scale, sheet Argelès-sur-Mer/Cerbère (1097). BRGM, Orléans. Handbook by Laumonier, B., Calvet, M., Barbey, P.,
777 Guennoc, P., Lambert J., Lenoble, J.L., Wiazemsky, M., 149 p.
778
- 779 Calvet, M., Gunnell, Y., & Laumonier, B. (2021). Denudation history and palaeogeography of the Pyrenees and their
780 peripheral basins: an 84-million-year geomorphological perspective. *Earth-Science Reviews*, 215, 103436.
781 <https://doi.org/10.1016/j.earscirev.2020.103436>
782
- 783 Carmignani, L., & Kligfield, R. (1990). Crustal extension in the northern Apennines: The transition from compression
784 to extension in the Alpi Apuane Core Complex. *Tectonics*, 9(6), 1275–1303.
785 <https://doi.org/10.1029/TC009i006p01275>
786
- 787 Carozza, J.-M. & Delcaillau, B. (1999). L'enregistrement géomorphologique de la tectonique quaternaire par les
788 nappes alluviales: l'exemple du bassin de la têt (roussillon, france). *Comptes Rendus de l'Académie des Sciences-*
789 *Series IIA-Earth and Planetary Science* 329 (10), 735–740.
790
- 791 Carozza, J.-M., & Baize, S. (2004). L'escarpement de faille de la Têt est-il le résultat de la tectonique active Plio-
792 Pléistocène ou d'une exhumation Pléistocène? *Comptes Rendus Geoscience*, 336(3), 217–226.
793 <https://doi.org/10.1016/j.crte.2003.10.026>
794
- 795 Cederbom, C., Larson, S. Å., Tullborg, E.-L., & Stiberg, J.-P. (2000). Fission track thermochronology applied to
796 Phanerozoic thermotectonic events in central and southern Sweden. *Tectonophysics*, 316(1–2), 153–167.
797 [https://doi.org/10.1016/S0040-1951\(99\)00230-9](https://doi.org/10.1016/S0040-1951(99)00230-9)
798
- 799 Charvin, K., Gallagher, K., Hampson, G. L., & Labourdette, R. (2009). A Bayesian approach to inverse modelling of
800 stratigraphy, part 1: method. *Basin Research*, 21(1), 5–25. <https://doi.org/10.1111/j.1365-2117.2008.00369.x>
801
- 802 Chevrot, S., Sylvander, M., Diaz, J., Martin, R., Mouthereau, F., Manatschal, G., et al. (2018). The non-cylindrical
803 crustal architecture of the Pyrenees. *Scientific Reports*, 8(1). <https://doi.org/10.1038/s41598-018-27889-x>
804
- 805 Choukroune, P. (1989). The Ecors Pyrenean deep seismic profile reflection data and the overall structure of an
806 orogenic belt. *Tectonics*, 8(1), 23–39. <https://doi.org/10.1029/TC008i001p00023>
807
- 808 Clauzon, G., Aguilar, J.-P., Michaux, J. (1987). Le bassin pliocène du Roussillon (Pyrénées orientales, France):
809 exemple d'évolution géodynamique d'une ria méditerranéenne consécutive à la crise de salinité messinienne. *C. R.*
810 *Acad. Sci. Paris Ser. 2* (304), 585e590.
811
- 812 Clauzon, G. (1990). Restitution de l'évolution géodynamique néogène du bassin du Roussillon et de l'unité adjacente
813 des Corbières d'après les données écostratigraphiques et paléogéographiques. *Paleobiol. Cont.* 17, 125e155.
814
- 815 Clauzon, G., Le Strat, P., Duvail, C., Do Couto, D., Suc, J.-P., Molliex, S., et al. (2015). The Roussillon Basin (S.
816 France): A case-study to distinguish local and regional events between 6 and 3 Ma. *Marine and Petroleum Geology*,
817 66, 18–40. <https://doi.org/10.1016/j.marpetgeo.2015.03.012>
818
- 819 Cochelin, B., Chardon, D., Denèle, Y., Gumiaux, C., & Le Bayon, B. (2017). Vertical strain partitioning in hot
820 Variscan crust: Syn-convergence escape of the Pyrenees in the Iberian-Armorican syntax. *Bulletin de La Société*
821 *Géologique de France*, 188(6), 39. <https://doi.org/10.1051/bsgf/2017206>

- 822
823 Colgan, J. P., Dumitru, T. A., Reiners, P. W., Wooden, J. L., & Miller, E. L. (2006). Cenozoic Tectonic Evolution of
824 the Basin and Range Province in Northwestern Nevada. *American Journal of Science*, 306(8), 616–654.
825 <https://doi.org/10.2475/08.2006.02>
826
- 827 Colgan, Joseph P., Shuster, D. L., & Reiners, P. W. (2008). Two-phase Neogene extension in the northwestern Basin
828 and Range recorded in a single thermochronology sample. *Geology*, 36(8), 631. <https://doi.org/10.1130/G24897A.1>
829
- 830 Crider, J. G., & Pollard, D. D. (1998). Fault linkage: Three-dimensional mechanical interaction between echelon
831 normal faults. *Journal of Geophysical Research: Solid Earth*, 103(B10), 24373–24391.
832 <https://doi.org/10.1029/98JB01353>
833
- 834 Cruset, D., Vergés, J., Albert, R., Gerdes, A., Benedicto, A., Cantarero, I., & Travé, A. (2020). Quantifying
835 deformation processes in the SE Pyrenees using U–Pb dating of fracture-filling calcites. *Journal of the Geological*
836 *Society*, 177(6), 1186–1196. <https://doi.org/10.1144/jgs2020-014>
837
- 838 Curry, M. A. E., Barnes, J. B., & Colgan, J. P. (2016). Testing fault growth models with low-temperature
839 thermochronology in the northwest Basin and Range, USA: TESTING FAULT GROWTH MODELS WITH AHE.
840 *Tectonics*, 35(10), 2467–2492. <https://doi.org/10.1002/2016TC004211>
841
- 842 Curry, M. E., van der Beek, P., Huismans, R. S., Wolf, S. G., & Muñoz, J.-A. (2019). Evolving paleotopography and
843 lithospheric flexure of the Pyrenean Orogen from 3D flexural modeling and basin analysis. *Earth and Planetary*
844 *Science Letters*, 515, 26–37. <https://doi.org/10.1016/j.epsl.2019.03.009>
845
- 846 Curry, M. E., van der Beek, P., Huismans, R. S., Wolf, S. G., Fillon, C., & Muñoz, J.-A. (2021). Spatio-temporal
847 patterns of Pyrenean exhumation revealed by inverse thermo-kinematic modeling of a large thermochronologic data
848 set. *Geology*. <https://doi.org/10.1130/G48687.1>
849
- 850 Danišík, M., Štěpančíková, P., & Evans, N. J. (2012). Constraining long-term denudation and faulting history in
851 intraplate regions by multisystem thermochronology: An example of the Sudetic Marginal Fault (Bohemian Massif,
852 central Europe): THERMOCHRONOLOGY OF THE SUDETES. *Tectonics*, 31(2).
853 <https://doi.org/10.1029/2011TC003012>
854
- 855 Deeken, A., Sobel, E. R., Coutand, I., Haschke, M., Riller, U., & Strecker, M. R. (2006). Development of the southern
856 Eastern Cordillera, NW Argentina, constrained by apatite fission track thermochronology: From early Cretaceous
857 extension to middle Miocene shortening: EXHUMING THE SOUTHEASTERN ANDES. *Tectonics*, 25(6).
858 <https://doi.org/10.1029/2005TC001894>
859
- 860 Delcaillau, B., Carozza, J.-M., & Font, M. (2004). The northern segment of the Têt Fault (Pyrenees-Orientales) :
861 Neogene evolution and geomorphic implications. *Bulletin de la Société Géologique de France*, 175(3), 257–272.
862 <https://doi.org/10.2113/175.3.257>
863
- 864 Delmas, M., Calvet, M., Gunnell, Y., Voinchet, P., Manel, C., Braucher, R., et al. (2018). Terrestrial ¹⁰Be and electron
865 spin resonance dating of fluvial terraces quantifies quaternary tectonic uplift gradients in the eastern Pyrenees.
866 *Quaternary Science Reviews*, 193, 188–211. <https://doi.org/10.1016/j.quascirev.2018.06.001>
867
- 868 Diaz, J., Vergés, J., Chevrot, S., Antonio-Vigil, A., Ruiz, M., Sylvander, M., & Gallart, J. (2018). Mapping the crustal
869 structure beneath the eastern Pyrenees. *Tectonophysics*, 744, 296–309. <https://doi.org/10.1016/j.tecto.2018.07.011>
870
- 871 Ehlers, T. A., & Farley, K. A. (2003). Apatite (U–Th)/He thermochronometry: methods and applications to problems
872 in tectonic and surface processes. *Earth and Planetary Science Letters*, 206(1–2), 1–14. [https://doi.org/10.1016/S0012-821X\(02\)01069-5](https://doi.org/10.1016/S0012-821X(02)01069-5)
873
- 874
- 875 Farley, K. A., Wolf, R. A., and Silver, L. T. (1996). The effects of long alpha-stopping distances on (U–Th)/He ages,
876 *Geochim. Cosmochim. Ac.*, 60, 4223–4229, [https://doi.org/10.1016/S0016-7037\(96\)00193-7](https://doi.org/10.1016/S0016-7037(96)00193-7)
877

- 878 Farley, K. A. (2002). (U-Th)/He Dating: Techniques, Calibrations, and Applications. *Reviews in Mineralogy and*
879 *Geochemistry*, 47(1), 819–844. <https://doi.org/10.2138/rmg.2002.47.18>
880
- 881 Faulkner, D. R., Jackson, C. A. L., Lunn, R. J., Schlische, R. W., Shipton, Z. K., Wibberley, C. A. J., & Withjack, M.
882 O. (2010). A review of recent developments concerning the structure, mechanics and fluid flow properties of fault
883 zones. *Journal of Structural Geology*, 32(11), 1557–1575. <https://doi.org/10.1016/j.jsg.2010.06.009>
884
- 885 Fillon, C., & van der Beek, P. (2012). Post-orogenic evolution of the southern Pyrenees: constraints from inverse
886 thermo-kinematic modelling of low-temperature thermochronology data. *Basin Research*, 24(4), 418–436.
887 <https://doi.org/10.1111/j.1365-2117.2011.00533.x>
888
- 889 Fillon, C., Mouthereau, F., Calassou, S., Pik, R., Bellahsen, N., Gautheron, C., ... & van der Beek, P. (2021). Post-
890 orogenic exhumation in the western Pyrenees: evidence for extension driven by pre-orogenic inheritance. *Journal of*
891 *the Geological Society*, 178(2). <https://doi.org/10.1144/jgs2020-079>
892
- 893 Fitzgerald, P. G., Sorkhabi, R. B., Redfield, T. F., & Stump, E. (1995). Uplift and denudation of the central Alaska
894 Range: A case study in the use of apatite fission track thermochronology to determine absolute uplift parameters.
895 *Journal of Geophysical Research: Solid Earth*, 100(B10), 20175–20191. <https://doi.org/10.1029/95JB02150>
896
- 897 Fitzgerald, P. G., Muñoz, J. A., Coney, P. J., & Baldwin, S. L. (1999). Asymmetric exhumation across the Pyrenean
898 orogen: implications for the tectonic evolution of a collisional orogen. *Earth and Planetary Science Letters*, 173(3),
899 157–170. [https://doi.org/10.1016/S0012-821X\(99\)00225-3](https://doi.org/10.1016/S0012-821X(99)00225-3)
900
- 901 Fitzgerald, P. G., & Malusà, M. G. (2019). Concept of the Exhumed Partial Annealing (Retention) Zone and Age-
902 Elevation Profiles in Thermochronology. In M. G. Malusà & P. G. Fitzgerald (Eds.), *Fission-Track Thermochronology*
903 *and its Application to Geology* (pp. 165–189). Cham: Springer International Publishing. [https://doi.org/10.1007/978-](https://doi.org/10.1007/978-3-319-89421-8_9)
904 [3-319-89421-8_9](https://doi.org/10.1007/978-3-319-89421-8_9)
905
- 906 Foster, D. A., & John, B. E. (1999). Quantifying tectonic exhumation in an extensional orogen with thermochronology:
907 examples from the southern Basin and Range Province. *Geological Society, London, Special Publications*, 154(1),
908 343–364. <https://doi.org/10.1144/GSL.SP.1999.154.01.16>
909
- 910 Gallagher, K., Charvin, K., Nielsen, S., Sambridge, M., & Stephenson, J. (2009). Markov chain Monte Carlo (MCMC)
911 sampling methods to determine optimal models, model resolution and model choice for Earth Science problems.
912 *Marine and Petroleum Geology*, 26(4), 525–535. <https://doi.org/10.1016/j.marpetgeo.2009.01.003>
913
- 914 Gallagher, K. (2012). Transdimensional inverse thermal history modeling for quantitative thermochronology. *Journal*
915 *of Geophysical Research: Solid Earth*, 117(B2). <https://doi.org/10.1029/2011JB008825>
916
- 917 Gautheron, C., Tassan-Got, L., Barbarand, J., & Pagel, M. (2009). Effect of alpha-damage annealing on apatite (U-
918 Th)/He thermochronology. *Chemical Geology*, 266(3–4), 157–170. <https://doi.org/10.1016/j.chemgeo.2009.06.001>
919
- 920 Gautheron, C., & Tassan-Got, L. (2010). A Monte Carlo approach to diffusion applied to noble gas/helium
921 thermochronology. *Chemical Geology*, 273(3–4), 212–224. <https://doi.org/10.1016/j.chemgeo.2010.02.023>
922
- 923 Gautheron, C., Pinna-Jamme, R., Derycke, A., Ahadi, F., Sanchez, C., Haurine, F., et al. (2021). Analytical protocols
924 and performance for apatite and zircon (U-Th)/He analysis on quadrupole and magnetic sector mass spectrometer
925 systems between 2007 and 2020. *Geochronology*, 3(1), 351–370. <https://doi.org/10.5194/gchron-3-351-2021>
926
- 927 Gibson, M., Sinclair, H. D., Lynn, G. J., & Stuart, F. M. (2007). Late- to post-orogenic exhumation of the Central
928 Pyrenees revealed through combined thermochronological data and modelling. *Basin Research*, 19(3), 323–334.
929 <https://doi.org/10.1111/j.1365-2117.2007.00333.x>
930
- 931 Glotzbach, C., van der Beek, P. A., & Spiegel, C. (2011). Episodic exhumation and relief growth in the Mont Blanc
932 massif, Western Alps from numerical modelling of thermochronology data. *Earth and Planetary Science Letters*,
933 304(3–4), 417–430. <https://doi.org/10.1016/j.epsl.2011.02.020>

- 934
935 Goula, X., Olivera, C., Fleta, J., Grellet, B., Lindo, R., Rivera, L. A., et al. (1999). Present and recent stress regime in
936 the eastern part of the Pyrenees. *Tectonophysics*, 308(4), 487–502. [https://doi.org/10.1016/S0040-1951\(99\)00120-1](https://doi.org/10.1016/S0040-1951(99)00120-1)
937
- 938 Green PF, Duddy IR, Laslett GM, Hegarty KA, Gleadow AJW, Lovering JF (1989) Thermal annealing of fission
939 tracks in apatite, 4, quantitative modelling techniques and extension to geological timescale. *J Pet Geol* 12:111–114.
940 [https://doi.org/10.1016/0168-9622\(89\)90018-3](https://doi.org/10.1016/0168-9622(89)90018-3)
941
- 942 Green, P. F., Crowhurst, P. V., Duddy, I. R., Japsen, P., & Holford, S. P. (2006). Conflicting (U–Th)/He and fission
943 track ages in apatite: Enhanced He retention, not anomalous annealing behaviour. *Earth and Planetary Science Letters*,
944 250(3–4), 407–427. <https://doi.org/10.1016/j.epsl.2006.08.022>
945
- 946 Grool, A. R., Ford, M., Vergés, J., Huisman, R. S., Christophoul, F., & Dielforder, A. (2018). Insights Into the
947 Crustal-Scale Dynamics of a Doubly Vergent Orogen From a Quantitative Analysis of Its Forelands: A Case Study of
948 the Eastern Pyrenees. *Tectonics*, 37(2), 450–476. <https://doi.org/10.1002/2017TC004731>
949
- 950 Guenther, W. R., Reiners, P. W., Ketcham, R. A., Nasdala, L., & Giester, G. (2013). Helium diffusion in natural
951 zircon: Radiation damage, anisotropy, and the interpretation of zircon (U–Th)/He thermochronology. *American*
952 *Journal of Science*, 313(3), 145–198. <https://doi.org/10.2475/03.2013.01>
953
- 954 Guitard, G., Geysant, J., Laumonier, B., Autran, A., Fontelles, M., Dalmayrac, B., Vidal, J., Bandet, Y. (1992). Carte
955 géologique de la France (1/50 000), feuille prades (1095).
956
- 957 Guitard, G., Laumonier, B., Autran, A., Bandet, Y., Berger, G. (1998). Notice explicative, carte géologique France
958 (1/50.000), feuille prades (1095). BRGM, Orléans.
959
- 960 Gunnell, Y., Calvet, M., Brichau, S., Carter, A., Aguilar, J.-P., & Zeyen, H. (2009). Low long-term erosion rates in
961 high-energy mountain belts: Insights from thermo- and biochronology in the Eastern Pyrenees. *Earth and Planetary*
962 *Science Letters*, 278(3–4), 208–218. <https://doi.org/10.1016/j.epsl.2008.12.004>
963
- 964 Hoareau, G., Crognier, N., Lacroix, B., Aubourg, C., Roberts, N. M. W., Niemi, N., et al. (2021). Combination of $\Delta 47$
965 and U–Pb dating in tectonic calcite veins unravel the last pulses related to the Pyrenean Shortening (Spain). *Earth and*
966 *Planetary Science Letters*, 553, 116636. <https://doi.org/10.1016/j.epsl.2020.116636>
967
- 968 Hurford, A. J. (1990). Standardization of fission track dating calibration: Recommendation by the Fission Track
969 Working Group of the I.U.G.S. Subcommittee on Geochronology. *Chemical Geology: Isotope Geoscience Section*,
970 80(2), 171–178. [https://doi.org/10.1016/0168-9622\(90\)90025-8](https://doi.org/10.1016/0168-9622(90)90025-8)
971
- 972 Huyghe, D., Mouthereau, F., Ségalen, L., & Furió, M. (2020). Long-term dynamic topographic support during post-
973 orogenic crustal thinning revealed by stable isotope ($\delta 18O$) paleo-altimetry in eastern Pyrenees. *Scientific Reports*,
974 10(1), 2267. <https://doi.org/10.1038/s41598-020-58903-w>
975
- 976 Jolivet, L., & Faccenna, C. (2000). Mediterranean extension and the Africa-Eurasia collision. *Tectonics*, 19(6), 1095–
977 1106. <https://doi.org/10.1029/2000TC900018>
978
- 979 Jolivet, L., Gorini, C., Smit, J., & Leroy, S. (2015). Continental breakup and the dynamics of rifting in back-arc basins:
980 The Gulf of Lion margin. *Tectonics*, 34(4), 662–679. <https://doi.org/10.1002/2014TC003570>
981
- 982 Jolivet, L., Romagny, A., Gorini, C., Maillard, A., Thinon, I., Couëffé, R., et al. (2020). Fast dismantling of a mountain
983 belt by mantle flow: Late-orogenic evolution of Pyrenees and Liguro-Provençal rifting. *Tectonophysics*, 776, 228312.
984 <https://doi.org/10.1016/j.tecto.2019.228312>
985
- 986 Jolivet, L., Menant, A., Roche, V., Le Pourhiet, L., Maillard, A., Augier, R., et al. (2021a). Transfer zones in
987 Mediterranean back-arc regions and tear faults. *BSGF - Earth Sciences Bulletin*, 192, 11.
988 <https://doi.org/10.1051/bsgf/2021006>

- 989 Jolivet, L., Baudin, T., Calassou, S., Chevrot, S., Ford, M., Issautier, B., et al. (2021b). Geodynamic evolution of a
 990 wide plate boundary in the Western Mediterranean, near-field versus far-field interactions. *BSGF - Earth Sciences*
 991 *Bulletin*, 192, 48. <https://doi.org/10.1051/bsgf/2021043>
 992
- 993 Jolivet, M., Labaume, P., Monié, P., Brunel, M., Arnaud, N., & Campani, M. (2007). Thermochronology constraints
 994 for the propagation sequence of the south Pyrenean basement thrust system (France-Spain): PROPAGATION OF
 995 THE SOUTH PYRENEAN PRISM. *Tectonics*, 26(5). <https://doi.org/10.1029/2006TC002080>
 996
- 997 Jones, C. H., & Wesnousky, S. G. (1992). Variations in Strength and Slip Rate Along the San Andreas Fault System.
 998 *Science*, 256(5053), 83–86. <https://doi.org/10.1126/science.256.5053.83>
 999
- 1000 Kattenhorn, S. A., Aydin, A., & Pollard, D. D. (2000). Joints at high angles to normal fault strike: an explanation
 1001 using 3-D numerical models of fault-perturbed stress fields p. *Journal of Structural Geology*, 22(1), 1-23.
 1002 [https://doi.org/10.1016/S0191-8141\(99\)00130-3](https://doi.org/10.1016/S0191-8141(99)00130-3)
 1003
- 1004 Ketcham, Richard A., Donelick, R. A., & Carlson, W. D. (1999). Variability of apatite fission-track annealing kinetics;
 1005 III, Extrapolation to geological time scales. *American Mineralogist*, 84(9), 1235–1255. <https://doi.org/10.2138/am-1999-0903>
 1006
- 1007 Ketcham, R. A., Carter, A., Donelick, R. A., Barbarand, J., & Hurford, A. J. (2007). Improved modeling of fission-
 1008 track annealing in apatite. *American Mineralogist*, 92(5–6), 799–810. <https://doi.org/10.2138/am.2007.2281>
 1009
- 1010 Ketcham, R. A., Gautheron, C., and Tassan-Got, L. (2011). Accounting for long alpha-particle stopping distances in
 1011 (U-Th-Sm)/He geochronology: Refinement of the baseline case, *Geochim. Cosmochim. Ac.*, 75, 7779–7791,
 1012 <https://doi.org/10.1016/j.gca.2011.10.011>
 1013
- 1014 Krugh, W. C. (2008). Low-temperature thermochronologic constraints on fault array evolution and patterns of range-
 1015 scale denudation. *ETH Zurich*. <https://doi.org/10.3929/ETHZ-A-005772437>
 1016
- 1017 Labaume, P., Meresse, F., Jolivet, M., Teixell, A., & Lahfid, A. (2016). Tectonothermal history of an exhumed thrust-
 1018 sheet-top basin: An example from the south Pyrenean thrust belt: JACA THRUST-SHEET-TOP BASIN. *Tectonics*,
 1019 35(5), 1280–1313. <https://doi.org/10.1002/2016TC004192>
 1020
- 1021 Lacan, P., & Ortuño, M. (2012). Active Tectonics of the Pyrenees: A review. *Journal of Iberian Geology*, 38(1).
 1022 https://doi.org/10.5209/rev_JIGE.2012.v38.n1.39203
 1023
- 1024 Lacombe, O., & Jolivet, L. (2005). Structural and kinematic relationships between Corsica and the Pyrenees-Provence
 1025 domain at the time of the Pyrenean orogeny: CORSICA AND PROVENCE IN THE LATE EOCENE. *Tectonics*,
 1026 24(1). <https://doi.org/10.1029/2004TC001673>
 1027
- 1028 Laumonier, B., Calvet, M., Le Bayon, B., Barbey, P., Lenoble, J.-L. (2015). avec la collaboration de Cocherie A.,
 1029 Melleton J. – Notice explicative, Carte géologique de la France à 1/50 000, feuille Prats-de-Mollo-la-Preste (1099).
 1030 In: Orléans : BRGM, page 189.
 1031
- 1032 Laumonier, B., Calvet, M., Delmas, M., Barbey, P., Lenoble, J., Autran, A. (2017). Notice explicative Carte
 1033 géologique de la France `a 1/50 000, feuille Mont-Louis (1094). In: Orléans : BRGM, page 139.
 1034
- 1035 Lewis, C. J., Vergés, J., & Marzo, M. (2000). High mountains in a zone of extended crust: Insights into the Neogene-
 1036 Quaternary topographic development of northeastern Iberia. *Tectonics*, 19(1), 86–102.
 1037 <https://doi.org/10.1029/1999TC900056>
 1038
- 1039 Malusà, M. G., Polino, R., Zattin, M., Bigazzi, G., Martin, S., & Piana, F. (2005). Miocene to Present differential
 1040 exhumation in the Western Alps: Insights from fission track thermochronology. *Tectonics*, 24(3).
 1041 <https://doi.org/10.1029/2004TC001782>
 1042
- 1043

- 1044 Malusà, M. G., Polino, R., & Zattin, M. (2009). Strain partitioning in the axial NW Alps since the Oligocene: STRAIN
 1045 PARTITIONING IN THE AXIAL ALPS. *Tectonics*, 28(3). <https://doi.org/10.1029/2008TC002370>
 1046
- 1047 Martín-González, F., Barbero, L., Capote, R., Heredia, N., & Gallastegui, G. (2012). Interaction of two successive
 1048 Alpine deformation fronts: constraints from low-temperature thermochronology and structural mapping (NW Iberian
 1049 Peninsula). *International Journal of Earth Sciences*, 101(5), 1331–1342. <https://doi.org/10.1007/s00531-011-0712-9>
 1050
- 1051 Mauffret, A., Durand de Grossouvre, B., Tadeu Dos Reis, A., Gorini, C., & Necessian, A. (2001). Structural geometry
 1052 in the eastern Pyrenees and western Gulf of Lion (Western Mediterranean). *Journal of Structural Geology*, 23(11),
 1053 1701–1726. [https://doi.org/10.1016/S0191-8141\(01\)00025-6](https://doi.org/10.1016/S0191-8141(01)00025-6)
 1054
- 1055 Maurel, O., Brunel, M., & Monié, P. (2002). Exhumation cénozoïque des massifs du Canigou et de Mont-Louis
 1056 (Pyrénées orientales, France). *Comptes Rendus Geoscience*, 334(12), 941-948. [https://doi.org/10.1016/S1631-0713\(02\)01834-5](https://doi.org/10.1016/S1631-0713(02)01834-5)
 1057
- 1058 Maurel, O., Monié, P., Pik, R., Arnaud, N., Brunel, M., & Jolivet, M. (2008). The Meso-Cenozoic thermo-tectonic
 1059 evolution of the Eastern Pyrenees: an ⁴⁰Ar/³⁹Ar fission track and (U–Th)/He thermochronological study of the
 1060 Canigou and Mont-Louis massifs. *International Journal of Earth Sciences*, 97(3), 565–584.
 1061 <https://doi.org/10.1007/s00531-007-0179-x>
 1062
- 1063 McDannell, K. T., Toro, J., Hourigan, J. K., & Harris, D. (2014). Thermochronologic constraints on Late Cretaceous
 1064 to Cenozoic exhumation of the Bendeleben Mountains, Seward Peninsula, Alaska. *Geochemistry, Geophysics,
 1065 Geosystems*, 15(10), 4009–4023. <https://doi.org/10.1002/2014GC005424>
 1066
- 1067 McCaig, A. M., & Miller, J. A. (1986). ⁴⁰Ar-³⁹Ar age of mylonites along the Merens Fault, central Pyrenees.
 1068 *Tectonophysics*, 129(1–4), 149–172. [https://doi.org/10.1016/0040-1951\(86\)90250-7](https://doi.org/10.1016/0040-1951(86)90250-7)
 1069
- 1070 McDowell, F. W., McIntosh, W. C., and Farley, K. A. (2005). A precise ⁴⁰Ar–³⁹Ar reference age for the Durango
 1071 apatite (U–Th)/He and fission-track dating standard, *Chem. Geol.*, 214, 249–263.
 1072 <https://doi.org/10.1016/j.chemgeo.2004.10.002>
 1073
- 1074 Medialdea, T., Vázquez, J., Vegas, R. (1994). Estructura y evolucion geodinamica del extremo noreste del margen
 1075 continental catalán durante el néogeno. *Acta Geol. Hisp.* 29 (2-4), 39–53.
 1076
- 1077 Metcalf, J. R., Fitzgerald, P. G., Baldwin, S. L., & Muñoz, J.-A. (2009). Thermochronology of a convergent orogen:
 1078 Constraints on the timing of thrust faulting and subsequent exhumation of the Maladeta Pluton in the Central Pyrenean
 1079 Axial Zone. *Earth and Planetary Science Letters*, 287(3–4), 488–503. <https://doi.org/10.1016/j.epsl.2009.08.036>
 1080
- 1081 Milesi, G., Soliva, R., Monié, P., Münch, P., Bellanger, M., Bruguier, O., et al. (2019a). Mapping a geothermal
 1082 anomaly using apatite (U–Th)/He thermochronology in the Têt fault damage zone, eastern Pyrenees, France. *Terra
 1083 Nova*, 31(6), 569–576. <https://doi.org/10.1111/ter.12429>
 1084
- 1085 Milesi, G. (2020). Analyse thermochronologique, géochimique et structurale du système hydrothermal de la faille de
 1086 la Têt (Pyrénées, France), un nouvel outil d’exploration géothermique. PhD thesis. Université de Montpellier.
 1087
- 1088 Milesi, G., Monié, P., Soliva, R., Münch, P., Taillefer, A., Bellanger, M., et al. (2020a). Imaging Geothermal
 1089 Anomalies Using Low-temperature (U–Th)/He Thermochronometry: A Case Study from the Active Têt Fault
 1090 Hydrothermal System (Eastern Pyrenees, France). In *Proceedings World Geothermal Congress 2020 Reykjavik,
 1091 Iceland, April 26–May 2, 2020*.
 1092
- 1093 Milesi, G., Monié, P., Münch, P., Soliva, R., Taillefer, A., Bruguier, O., et al. (2020b). Tracking geothermal anomalies
 1094 along a crustal fault using (U – Th)/He apatite thermochronology and rare-earth element (REE) analyses: the example
 1095 of the Têt fault (Pyrenees, France). *Solid Earth*, 11(5), 1747–1771. <https://doi.org/10.5194/se-11-1747-2020>
 1096
- 1097 Morris, R.G., Sinclair, H.D. and Yelland, A.J. (1998). Exhumation of the Pyrenean orogen: implications for sediment
 1098 discharge. *Basin Research*, 10, 69–86, <https://doi.org/10.1046/j.1365-2117.1998.00053.x>
 1099

- 1100
 1101 Mouthereau, F., Filleaudeau, P.-Y., Vacherat, A., Pik, R., Lacombe, O., Fellin, M. G., et al. (2014). Placing limits to
 1102 shortening evolution in the Pyrenees: Role of margin architecture and implications for the Iberia/Europe convergence:
 1103 Plate convergence in the Pyrenees. *Tectonics*, 33(12), 2283–2314. <https://doi.org/10.1002/2014TC003663>
 1104
- 1105 Mouthereau, F., Angrand, P., Jourdon, A., Ternois, S., Fillon, C., Calassou, S., et al. (2021). Cenozoic mountain
 1106 building and topographic evolution in Western Europe: impact of billions of years of lithosphere evolution and plate
 1107 kinematics. *BSGF - Earth Sciences Bulletin*, 192, 56. <https://doi.org/10.1051/bsgf/2021040>
 1108
- 1109 Muñoz, J. A. (1992). Evolution of a continental collision belt: ECORS-Pyrenees crustal balanced cross-section. In K.
 1110 R. McClay (Ed.), *Thrust Tectonics* (pp. 235–246). Dordrecht: Springer Netherlands. [https://doi.org/10.1007/978-94-
 1111 011-3066-0_21](https://doi.org/10.1007/978-94-011-3066-0_21)
 1112
- 1113 Nercessian, A., Mau, A., Gallart, J., & Diaz, J. (2001). Deep reflection seismic images of the crustal thinning in the
 1114 eastern Pyrenees and western Gulf of Lion. *Journal of Geodynamics*, 15. [https://doi.org/10.1016/S0264-
 1115 3707\(00\)00029-6](https://doi.org/10.1016/S0264-3707(00)00029-6)
 1116
- 1117 Norris, R. J., & Cooper, A. F. (2001). Late Quaternary slip rates and slip partitioning on the Alpine Fault, New Zealand.
 1118 *Journal of Structural Geology*, 23(2–3), 507–520. [https://doi.org/10.1016/S0191-8141\(00\)00122-X](https://doi.org/10.1016/S0191-8141(00)00122-X)
 1119
- 1120 Parizot, O., Missenard, Y., Haurine, F., Blaise, T., Barbarand, J., Benedicto, A., & Sarda, P. (2021). When did the
 1121 Pyrenean shortening end? Insight from U–Pb geochronology of syn-faulting calcite (Corbières area, France). *Terra
 1122 Nova*, 33(6), 551–559. <https://doi.org/10.1111/ter.12547>
 1123
- 1124 Petit, C., & Mouthereau, F. (2012). Steep topographic slope preservation by anisotropic diffusion: An example from
 1125 the Neogene Têt fault scarp, eastern Pyrenees. *Geomorphology*, 171–172, 173–179.
 1126 <https://doi.org/10.1016/j.geomorph.2012.05.016>
 1127
- 1128 Pous, J., Julià, R., Sagrañes, L.S. (1986). Cerdanya basin geometry and its implication on the neocene evolution of
 1129 the eastern pyrenees. *Tectonophysics* 129 (1–4), 355–365. [https://doi.org/10.1016/0040-1951\(86\)90261-1](https://doi.org/10.1016/0040-1951(86)90261-1)
 1130
- 1131 Price, J. G., & Henry, C. D. (1984). Stress orientations during Oligocene volcanism in Trans-Pecos Texas: Timing the
 1132 transition from Laramide compression to Basin and Range tension. *Geology*, 12(4), 238–241.
 1133 [https://doi.org/10.1130/0091-7613\(1984\)12<238:SODOVI>2.0.CO;2](https://doi.org/10.1130/0091-7613(1984)12<238:SODOVI>2.0.CO;2)
 1134
- 1135 Ratschbacher, L., Hacker, B. R., Calvert, A., Webb, L. E., Grimmer, J. C., McWilliams, M. O., et al. (2003). Tectonics
 1136 of the Qinling (Central China): tectonostratigraphy, geochronology, and deformation history. *Tectonophysics*, 366(1–
 1137 2), 1–53. [https://doi.org/10.1016/S0040-1951\(03\)00053-2](https://doi.org/10.1016/S0040-1951(03)00053-2)
 1138
- 1139 Rehault, J., Moussat, E., Fabbri, A. (1987). Structural evolution of the tyrrhenian back-arc basin. *Mar. Geol.* 74 (1-2),
 1140 123–150. [https://doi.org/10.1016/0025-3227\(87\)90010-7](https://doi.org/10.1016/0025-3227(87)90010-7)
 1141
- 1142 Reiners, P.W., Farley, K.A., and Hiskes, H.J. (2002). He diffusion and (U-Th)/He thermochronology of zircon: initial
 1143 results from Fish Canyon Tuff and Gold Butte. *Tectonophysics*, 349: 297-308, [https://doi.org/10.1016/S0040-
 1144 1951\(02\)00058-6](https://doi.org/10.1016/S0040-1951(02)00058-6)
 1145
- 1146 Reiners, P. W., & Brandon, M. T. (2006). USING THERMOCHRONOLOGY TO UNDERSTAND OROGENIC
 1147 EROSION. *Annual Review of Earth and Planetary Sciences*, 34(1), 419–466.
 1148 <https://doi.org/10.1146/annurev.earth.34.031405.125202>
 1149
- 1150 Reiners, P. W. (2007). Thermochronologic Approaches to Paleotopography. *Reviews in Mineralogy and
 1151 Geochemistry*, 66(1), 243–267. <https://doi.org/10.2138/rmg.2007.66.10>
 1152
- 1153 Reiners, P. W., and S. Nicolescu (2006), Measurement of parent nuclides for (U-Th)/He chronometry by solution
 1154 sector ICP-MS, ARHDL Rep., 1, Ariz. Radiogenic Helium Dating Lab., Tucson. Available at
 1155 https://www.geo.arizona.edu/~reiners/arhdl/U-Th-Sm_measurement_Reiners_042107.pdf

- 1156
1157 Rigo, A., Vernant, P., Feigl, K. L., Goula, X., Khazaradze, G., Talaya, J., et al. (2015). Present-day deformation of
1158 the Pyrenees revealed by GPS surveying and earthquake focal mechanisms until 2011. *Geophysical Journal*
1159 *International*, 201(2), 947–964. <https://doi.org/10.1093/gji/ggv052>
1160
- 1161 Roca, E. & Santanach, P. (1986). Génesis y evolucion de la Fosa de la Cerdanya (Pirineos orientales). *Geogaceta* 1,
1162 37–38.
1163
- 1164 Roca, E. & Desegaulx, P. (1992). Analysis of the geological evolution and vertical movements in the valencia trough
1165 area, western mediterranean. *Marine and Petroleum Geology*, 9(2) :167–176.
1166
- 1167 Roca, E. (1996). The Neogene Cerdanya and Seu d’Urgell intramontane basins (eastern Pyrenees). In: Friend, P.,
1168 Bario, C.J. (Eds.), *Tertiary Basins of Spain. The Stratigraphic Record of Crustal Kinematics*. Cambridge University
1169 Press, Cambridge, pp. 114–118.
1170
- 1171 Romagny, A., Jolivet, L., Menant, A., Bessière, E., Maillard, A., Canva, A., et al. (2020). Detailed tectonic
1172 reconstructions of the Western Mediterranean region for the last 35 Ma, insights on driving mechanisms. *BSGF -*
1173 *Earth Sciences Bulletin*, 191, 37. <https://doi.org/10.1051/bsgf/2020040>
1174
- 1175 Roure, F., Choukroune, P., Berastegui, X., Munoz, J. A., Villien, A., Matheron, P., et al. (1989). Ecore deep seismic
1176 data and balanced cross sections: Geometric constraints on the evolution of the Pyrenees. *Tectonics*, 8(1), 41–50.
1177 <https://doi.org/10.1029/TC008i001p00041>
1178
- 1179 Rushlow, C. R., Barnes, J. B., Ehlers, T. A., & Vergés, J. (2013). Exhumation of the southern Pyrenean fold-thrust
1180 belt (Spain) from orogenic growth to decay: EXHUMATION OF THE SOUTHERN PYRENEES. *Tectonics*, 32(4),
1181 843-860. <https://doi.org/10.1002/tect.20030>
1182
- 1183 Sambridge, M. (1999). Geophysical inversion with a neighbourhood algorithm - II. Appraising the ensemble.
1184 *Geophysical Journal International*, 138, 727-746. <https://doi.org/10.1046/j.1365-246x.1999.00900.x>
1185
- 1186 Sartégou, A., Bourlès, D. L., Blard, P.-H., Braucher, R., Tibari, B., Zimmermann, L., et al. (2018). Deciphering
1187 landscape evolution with karstic networks: A Pyrenean case study. *Quaternary Geochronology*, 43, 12–29.
1188 <https://doi.org/10.1016/j.quageo.2017.09.005>
1189
- 1190 Saula, E., Picart, J., Mató, E., Llenas, M., Losantos, M., Berástegui, X., & Agustí, J. (1994). Evolución geodinámica
1191 de la fosa del Empordà y las Sierras Transversales. *Acta geológica hispánica*, 29(2-4), 55-75.
1192
- 1193 Schmitz, M.D. & Bowring, S.A. (2001). U-Pb zircon and titanite systematics of the Fish Canyon Tuff: an assessment
1194 of high precision U-Pb geochronology and its application to young volcanic rocks. *Geochim. Cosmochim. Acta*, 65:
1195 2571-2587, [https://doi.org/10.1016/S0016-7037\(01\)00616-0](https://doi.org/10.1016/S0016-7037(01)00616-0)
1196
- 1197 Schwarz, G. (1978). Estimating the dimension of a model. *The annals of statistics*, 6(2), 461-464.
1198
- 1199 Séranne, M., Benedicto, A., Labaum, P., Truffert, C., & Pascal, G. (1995). Structural style and evolution of the Gulf
1200 of Lion Oligo-Miocene rifting: Role of the Pyrenean orogeny. *Marine and Petroleum geology*, 12(8), 809-820.
1201 [https://doi.org/10.1016/0264-8172\(95\)98849-Z](https://doi.org/10.1016/0264-8172(95)98849-Z)
1202
- 1203 Séranne, M. (1999). The Gulf of Lion continental margin (NW Mediterranean) revisited by IBS: an overview.
1204 *Geological Society, London, Special Publications*, 156(1), 15–36. <https://doi.org/10.1144/GSL.SP.1999.156.01.03>
1205
- 1206 Séranne, M., Couëffé, R., Husson, E., Baral, C., & Villard, J. (2021). The transition from Pyrenean shortening to Gulf
1207 of Lion rifting in Languedoc (South France)—A tectonic-sedimentation analysis. *BSGF-Earth Sciences Bulletin*,
1208 192(1), 27. <https://doi.org/10.1051/bsgf/2021017>
1209
- 1210 Sibuet, J.-C., Srivastava, S. P., & Spakman, W. (2004). Pyrenean orogeny and plate kinematics. *Journal of*
1211 *Geophysical Research: Solid Earth*, 109(B8). <https://doi.org/10.1029/2003JB002514>

- 1212
1213 Sinclair, H. D., Gibson, M., Naylor, M., & Morris, R. G. (2005). Asymmetric growth of the Pyrenees revealed through
1214 measurement and modeling of orogenic fluxes. *American Journal of Science*, 305(5), 369–406.
1215 <https://doi.org/10.2475/ajs.305.5.369>
1216
- 1217 Stockli, D. F., Farley, K. A., & Dumitru, T. A. (2000). Calibration of the apatite (U-Th)/He thermochronometer on an
1218 exhumed fault block, White Mountains, California. *Geology*, 28(11), 983–986. [https://doi.org/10.1130/0091-7613\(2000\)28<983:COTAHT>2.0.CO;2](https://doi.org/10.1130/0091-7613(2000)28<983:COTAHT>2.0.CO;2)
1219
- 1220
1221 Stockli, D. F. (2005). Application of Low-Temperature Thermochronometry to Extensional Tectonic Settings.
1222 *Reviews in Mineralogy and Geochemistry*, 58(1), 411–448. <https://doi.org/10.2138/rmg.2005.58.16>
1223
- 1224 Stüwe, K., White, L., & Brown, R. (1994). The influence of eroding topography on steady-state isotherms. Application
1225 to fission track analysis. *Earth and Planetary Science Letters*, 124(1–4), 63–74. [https://doi.org/10.1016/0012-821X\(94\)00068-9](https://doi.org/10.1016/0012-821X(94)00068-9)
1226
- 1227
1228 Surpless, B. E., Stockli, D. F., Dumitru, T. A., & Miller, E. L. (2002). Two-phase westward encroachment of Basin
1229 and Range extension into the northern Sierra Nevada: BASIN AND RANGE ENCROACHMENT. *Tectonics*, 21(1),
1230 2-1-2–10. <https://doi.org/10.1029/2000TC001257>
1231
- 1232 Taillefer, A., Soliva, R., Guillou-Frottier, L., Le Goff, E., Martin, G., & Séranne, M. (2017). Fault-Related Controls
1233 on Upward Hydrothermal Flow: An Integrated Geological Study of the Têt Fault System, Eastern Pyrénées (France).
1234 *Geofluids*, 2017, 1–19. <https://doi.org/10.1155/2017/8190109>
1235
- 1236 Taillefer, A., Milesi, G., Soliva, R., Monnier, L., Delorme, P., Guillou-Frottier, L., & Le Goff, E. (2021). Polyphased
1237 brittle deformation around a crustal fault: A multi-scale approach based on remote sensing and field data on the
1238 mountains surrounding the Têt hydrothermal system (Eastern Pyrénées, France). *Tectonophysics*, 804, 228710.
1239 <https://doi.org/10.1016/j.tecto.2020.228710>
1240
- 1241 Tassone, A., Roca, E., Muñoz, J. A., Cabrera, L., & Canals, M. (1994). Evolución del sector septentrional del margen
1242 continental catalán durante el Cenozoico. *Acta geológica hispánica*, 29(2-4), 3-37.
1243
- 1244 Teixell, A., Labaume, P., & Lagabrielle, Y. (2016). The crustal evolution of the west-central Pyrenees revisited:
1245 Inferences from a new kinematic scenario. *Comptes Rendus Geoscience*, 348(3–4), 257–267.
1246 <https://doi.org/10.1016/j.crte.2015.10.010>
1247
- 1248 Ternois, S., Odlum, M., Ford, M., Pik, R., Stockli, D., Tibari, B., et al. (2019). Thermochronological Evidence of
1249 Early Orogenesis, Eastern Pyrenees, France. *Tectonics*, 38(4), 1308–1336. <https://doi.org/10.1029/2018TC005254>
1250
- 1251 Tosal, A., Verduzco, O., & Martín-Closas, C. (2021). CLAMP-based palaeoclimatic analysis of the late Miocene
1252 (Tortonian) flora from La Cerdanya Basin of Catalonia, Spain, and an estimation of the palaeoaltitude of the eastern
1253 Pyrenees. *Palaeogeography, Palaeoclimatology, Palaeoecology*, 564, 110186.
1254 <https://doi.org/10.1016/j.palaeo.2020.110186>
1255
- 1256 Vacherat, A., Mouthereau, F., Pik, R., Huyghe, D., Paquette, J.-L., Christophoul, F., et al. (2016). Rift-to-collision
1257 sediment routing in the Pyrenees: A synthesis from sedimentological, geochronological and kinematic constraints.
1258 *Earth-Science Reviews*, 172, 43–74. <https://doi.org/10.1016/j.earscirev.2017.07.004>
1259
- 1260 Vergés, J., Millán, H., Roca, E., Muñoz, J. A., Marzo, M., Cirés, J., et al. (1995). Eastern Pyrenees and related foreland
1261 basins: pre-, syn- and post-collisional crustal-scale cross-sections. *Marine and Petroleum Geology*, 12(8), 903–915.
1262 [https://doi.org/10.1016/0264-8172\(95\)98854-X](https://doi.org/10.1016/0264-8172(95)98854-X)
1263
- 1264 Vergés, J., Fernandez, M., & Martínez, A. (2002). The Pyrenean orogen: Pre-, syn-, and post-collisional evolution.
1265 *Journal of the Virtual Explorer*, 08, 55–74. <https://doi.org/10.3809/jvirtex.2002.00058>
1266

- 1267 Vermeesch, P., & Tian, Y. (2014). Thermal history modelling: HeFTy vs. QTQt. *Earth-Science Reviews*, 139, 279–
 1268 290. <https://doi.org/10.1016/j.earscirev.2014.09.010>
 1269
- 1270 Vignaroli, G., Faccenna, C., Jolivet, L., Piromallo, C., & Rossetti, F. (2008). Subduction polarity reversal at the
 1271 junction between the Western Alps and the Northern Apennines, Italy. *Tectonophysics*, 450(1–4), 34–50.
 1272 <https://doi.org/10.1016/j.tecto.2007.12.012>
 1273
- 1274 Viola, G., Odone, F., & Mancktelow, N. S. (2004). Analogue modelling of reverse fault reactivation in strike–slip
 1275 and transpressive regimes: application to the Giudicarie fault system, Italian Eastern Alps. *Journal of Structural*
 1276 *Geology*, 26(3), 401–418. <https://doi.org/10.1016/j.jsg.2003.08.014>
 1277
- 1278 Wagner, G.A., Reimer, G.M., Jäger, E. (1977). Cooling ages derived by apatite fission track, mica Rb–Sr and K–Ar
 1279 dating: the uplift and cooling history of the central Alps. *Mem. Sci. Geol. Padova* 30, 1–27.
 1280
- 1281 Waldner, M., Bellahsen, N., Mouthereau, F., Bernet, M., Pik, R., Rosenberg, C. L., & Balvay, M. (2021). Central
 1282 Pyrenees Mountain Building: Constraints From New LT Thermochronological Data From the Axial Zone. *Tectonics*,
 1283 40(3). <https://doi.org/10.1029/2020TC006614>
 1284
- 1285 Wessel, P., Luis, J. F., Uieda, L., Scharroo, R., Wobbe, F., Smith, W. H. F., & Tian, D. (2019). The generic mapping
 1286 tools version 6. *Geochemistry, Geophysics, Geosystems*, 20(11), 5556–5564. <https://doi.org/10.1029/2019GC008515>
 1287
- 1288 Whitchurch, A. L., Carter, A., Sinclair, H. D., Duller, R. A., Whittaker, A. C., & Allen, P. A. (2011). Sediment routing
 1289 system evolution within a diachronously uplifting orogen: Insights from detrital zircon thermochronological analyses
 1290 from the South-Central Pyrenees. *American Journal of Science*, 311(5), 442–482. <https://doi.org/10.2475/05.2011.03>
 1291
- 1292 Wu, L., Monié, P., Wang, F., Lin, W., Ji, W., Bonno, M., Münch, P., and Wang, Q. (2016). Cenozoic exhumation
 1293 history of Sulu terrane: Implications from (U-Th)/He thermochrology, *Tectonophysics*, 672–673, 1–15,
 1294 <https://doi.org/10.1016/j.tecto.2016.01.035>
 1295
- 1296 Ziegler, P. A. (1992). European Cenozoic rift system. *Tectonophysics*, 208(1-3), 91-111.
 1297 [https://doi.org/10.1016/0040-1951\(92\)90338-7](https://doi.org/10.1016/0040-1951(92)90338-7)
 1298

1299 **References From the Supporting Information**

- 1300 Sun, S. S., and McDonough, W. F. (1989) Chemical and isotopic systematics of oceanic basalts: implications for
 1301 mantle composition and processes. Geological Society, London, Special Publications, 42, 313–345.
 1302 <https://doi.org/10.1144/GSL.SP.1989.042.01.19>
 1303